Effects of Concurrent Irradiation with Ions and Electrons on Cascade Damages in Non-metallic Inorganic Crystals

阿部, 弘亨
Graduate School of Engineering, Kyushu University

https://doi.org/10.11501/3065528

出版情報：九州大学, 1992, 博士（工学）, 課程博士
バージョン：
権利関係：

Effects of Concurrent Irradiation with Ions and Electrons on Cascade Damages in Non-metallic Inorganic Crystals

Hiroaki Abe

①

EFFECTS OF CONCURRENT IRRADIATION WITH IONS AND ELECTRONS ON CASCADE DAMAGES IN NON-METALLIC INORGANIC CRYSTALS

BY

HIROAKI ABE

GRADUATE SCHOOL OF ENGINEERING

KYUSHU UNIVERSITY

JANUARY 1993

TABLE OF CONTENTS

CHAPTER 1

INTRODUCTION

1.1. PREFACE

Non-metallic inorganic materials have been effectively used as fission reactor materials and are expected to be indispensable materials for fusion reactors. Examples are fuel and coating materials of fuel particle for fission reactors shown in **table 1.1** [1]. Also shown in **table 1.2** [2] are candidate materials for fusion reactors as low-Z first wall structures, diverter collectors, dielectrics for RF heating systems and others. Semiconductors are used as detectors and diagnostics in irradiation environments. Non-metallic inorganic materials such as ceramics and semiconductors are required to maintain their structural and electrical integrity under irradiation with neutrons, ions, electrons and γ rays in fusion reactors. However, our understanding on radiation damage in ceramic materials is not enough to develop irradiation resistant materials because of their complicated characteristics such as the atomic bonding, the mass of constituent atoms, electrical neutrality, structural vacancies and so on.

When materials are irradiated with energetic particles, they induce point defects, lattice vibration and electronic excitation, leading to the deterioration of properties of materials called radiation damage through nuclear and electronic energy loss processes. The nuclear energy loss process is described as energy transfer to primary knock-on atoms (PKAs) through the elastic collision. On the contrary, the electronic energy loss is done through the

Table 1.1. Examples of application of ceramics to fission reactor components [2].

Compornent	Ceramics
Fuel	UO_2, (U, Pu)O_2, ThO_2, (U, Th)O_2, UC and UN
Coating for fuel particles	C, SiC and ZrC
Moderator and Reflector	BeO, C and ZrH_2
Control Material	B_4C, Eu_2O_3 and Gd_2O_3
Shielding Material	B_4C, C, heavy concrete and lead glass
Pressure or Reactor Vessel	Prestressed concrete

Table 1.2. Examples of candidate ceramic materials for fusion reactor components together with their operating conditions, stress and special problems [1].

Component	Operating Conditions				Stress	Candidate Materials	Special Problems
	Neutron flux (n/m^2s)	Ionizing dose rate (Gy/s)	Temp. (°C)	Potential gradient (kV/mm)			
First wall	10^{19}	10^5	< 1200		High	SiC, Si_3N_4	Sputtering, errosion
Limiters	10^{19}	10^5	< 1200		High	Coated graphite	High transient temperatures, sputtering, errosion
Armor	10^{19}	10^5	< 1200		Medium	Coated graphite	High particle fluxes
Neutral beam injector insulator	$10^{14} \sim 10^{16}$	10	< 250	1 ~ 5	Medium	Al_2O_3, MgO, MACOR	Resistivity $>10^6$ Ωm
Troidal current break	$10^{16} \sim 10^{18}$	1 ~ 100	~ 500	< 1	High	Al_2O_3, $MgAl_2O_4$	
Shaping and diverter coil insulators	10^{18}	100	~ 500	~ 1	High	Al_2O_3, $MgAl_2O_4$	
Direct converter insulators	$10^{14} \sim 10^{16}$	> 10	~ 1000	~ 10	Low	Al_2O_3, MACOR	DC field could induce electrolysis failure
Windows for rf heating	$< 10^{19}$	$< 10^5$	~ 500	0.1 ~ 1	High	BeO, Al_2O_3	Loss tangent must be low

inelastic interaction which induces electronic excitation or ionization. The PKA energy (T) ranges from zero to its maximum (T_{max}) which depends on the energy of projectiles (E) and the combination of projectiles and target atoms. PKAs with energy less than the displacement threshold energy (E_d) induce no displacements and their energy dissipates mainly into phonon excitation (lattice vibration). The energy less than E_d contributes to athermal migration of point defects. When $T \geq E_d$, the number of displaced atoms is proportional to T below about A keV (A is the mass number of target atoms) and it levels off for higher values of T where the major part of the energy is lost through the electronic energy loss process. PKAs with relatively low energy produce freely migrating point defects (isolated point defects), which would result in nucleation and growth of defect clusters such as loops and voids. PKAs with energy more than the order of keV generate series of collisions which result in formation of cascade damages described as vacancy-rich cores surrounded by interstitials. A schematic example of cascade damages is shown in **figure 1.1**. Vacancies and interstitials in a cascade damage, in some cases, agglomerate and collapse into defect clusters almost spontaneously after the cascade generation. Those processes are dominated by the energy density, the defect distribution and the stability of cascade damages.

Generally, nuclear materials are subjected to irradiation with many kinds of energetic particles and the PKA energy spectrum varies widely in materials under neutron irradiation. In those materials, both of isolated point defects and cascade damages are simultaneously introduced and might induce concurrent or synergistic effects of them. **Figure 1.2** is examples of damage energy spectra of fission and fusion neutron irradiation in Ni as a function of

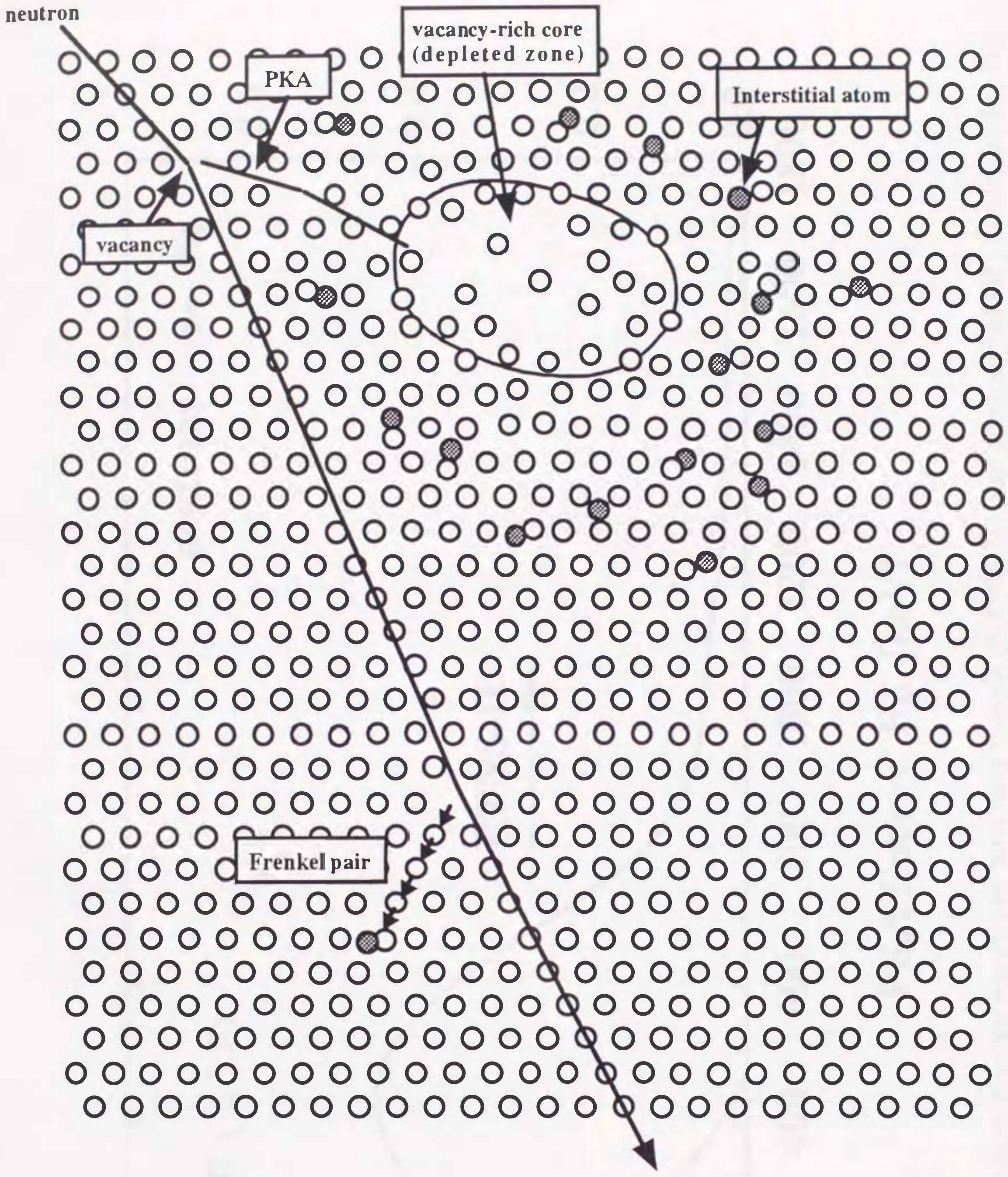

Figure 1.1 A schematic diagram showing the behavior of atoms along the trajectory of a fast neutron in a crystal. High energy primary knock-on atoms (PKAs) generate cascades consisting of vacancy-rich cores (depleted zones) surrounded with interstitial atoms. Lower energy PKAs generate isolated Frenkel pairs.

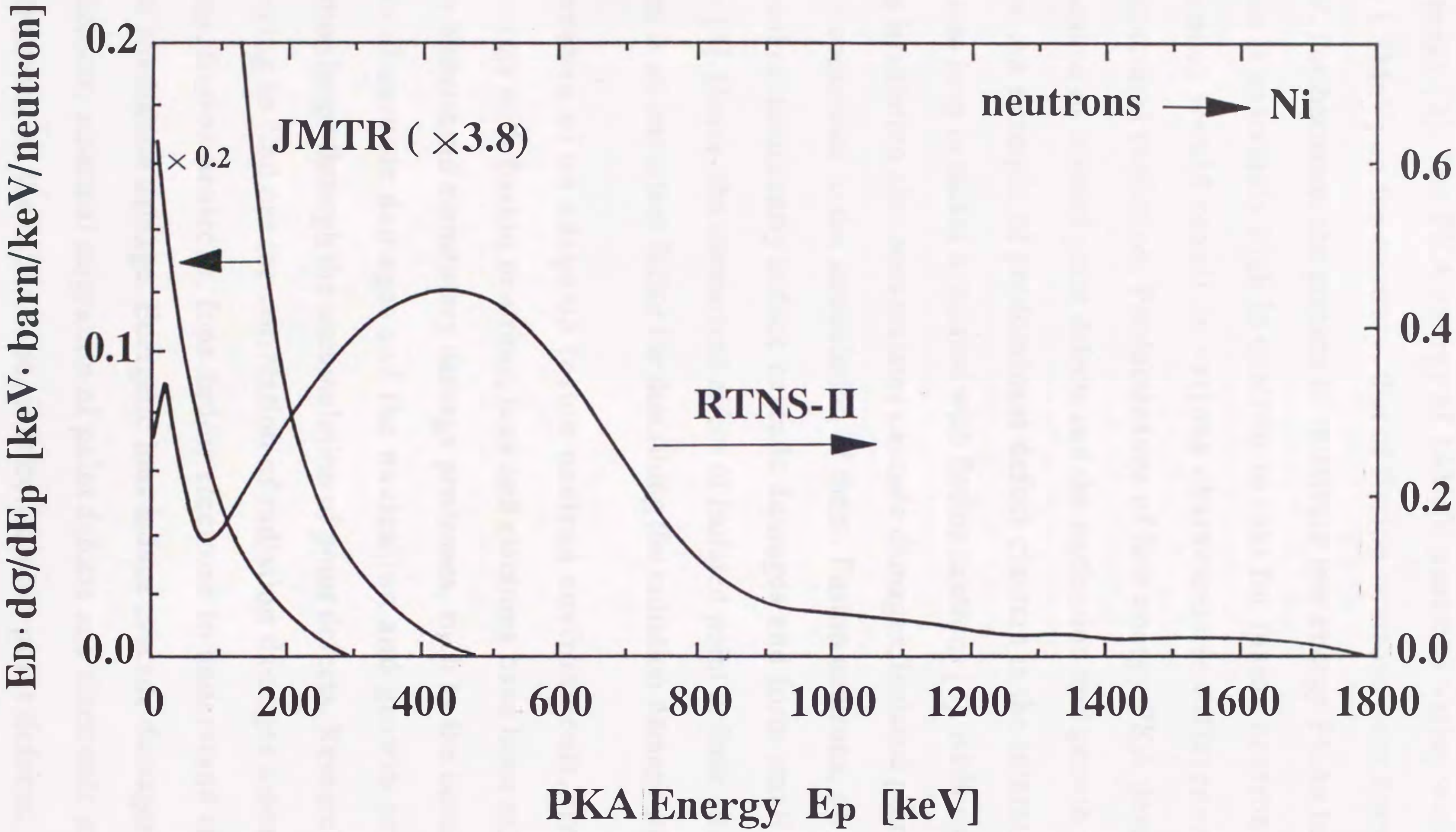

Figure 1.2 A comparison of damage energy spectrum between fusion (RTNS-II) and fission(JMTR) neutrons for Ni.

PKA energy [3]. The PKA energy of 14MeV neutrons varies widely from zero to 1.8MeV; on the contrary, that of fission neutrons does from zero to 0.5MeV. Furthermore, the portion of relatively low energy PKAs for fission neutrons is extremely high in contrast to that for fusion neutrons. These differences would result in various characteristic differences in the microstructural evolution. Predominance of low energy PKA develops the accumulation of isolated point defects and the nucleation and growth of defect clusters. An example of predominant defect clusters is the interstitial type dislocation loop in nickel irradiated with fission neutrons [3]. Although fission neutron irradiation also accumulates cascade damages, isolated point defects strongly contribute to the annihilation of them. Fusion neutrons, on the other hand, rather dominantly induce cascade damages and form small vacancy clusters [3]. Hence, the concurrent effect of isolated point defects and cascade damages is an important factor for describing the radiation damage process.

Because of no adequate fusion neutron environments, irradiation experiments with fission neutrons, ions and electrons have been extensively done to understand elementary damage processes, such as the accumulation process of cascade damages and the nucleation and growth process of dislocation loops through the accumulation of point defects. Researchers have been trying to find out the correlation of radiation damages among fusion neutrons, fission neutrons, ions and/or electrons to understand the fusion neutron irradiation damage. Energetic ions induce cascade damages, isolated point defects, athermal migration of point defects and electronic excitation. Fast electrons, on the other hand, induce isolated point defects, athermal migration of point defects and electronic excitation. Therefore, dual-beam irradiation with ions and electrons is expected to give an insight into the concurrent effects of cascade damages, isolated point defects, athermal migration of point defects and electronic excitation, and to give hints for finding out the correlation between fission and fusion neutron irradiation damages. High voltage electron microscopes combined with ion accelerators (HVEM-ACC) allow us to perform in-situ observation of the microstructural evolution under concurrent irradiation with ions and electrons. The variation of irradiation conditions, such as ion species, ion energy, electron energy and portion of ion and electron dose rates provides systematic experiments for getting insights into radiation damage processes and their synergistic effects under fusion irradiation environments.

1.2. REVIEW ON CONCURRENT IRRADIATION WITH IONS AND ELECTRONS

Transmission electron microscopes interfaced with ion accelerators have been developed for the purpose of in-situ observation of ion radiation damage in materials [4-27]. Most of them [19-27] are based on conventional transmission electron microscopes whose accelerating voltage ranges from 100 to 400 kV. The HVEM-ACC facility at University of Virginia [4] and the HVEM-TANDEM facility at Argonne National Laboratory [5-9] are the first equipments based on HVEM, and their major objectives were in-situ observation of thick specimens. As pointed out by Takeyama et al. [14], however, great advantages of HVEM-ACC facilities are based on dual-beam irradiation experiments under simultaneous observation. The dual-beam irradiation has raised scientific interest of several researchers [10-15,28-32].

Ohnuki et al. [15] have observed helium and/or electron irradiation effects on cavity formation in ferritic stainless steel. The microstructural change under dual-beam irradiation with helium and electrons is characterized as a bi-modal size distribution of cavities in contrast to the single mode distribution of them under irradiation with helium ions or electrons, showing remarkable stability of cavities with helium. Kimoto et al. [29] have found the dual-beam irradiation effects on loop growth in Fe-25Ni-15Cr-0.02C alloy.

Seidman et al. [28] have observed amorphization in Si under irradiation with ions at 10K and its retardation under simultaneous irradiation with electrons and ions. Electron irradiation assists Si in retaining crystallinity. The critical electron dose rate enough to retain crystallinity was determined as a function of ion dose rate, showing a linear relationship between the critical electron dose rate and ion dose rate. However, the linear relationship was not deduced at much less or higher ion dose rate region in their work. The retardation of amorphization during dual-beam irradiation with ions and electrons has been also reported by Ohnuki et al. [30].

Koike [32] has investigated the temperature dependence of the concurrent effect of dual-beam irradiation with ions and electrons on amorphization of intermetallic compounds. Irradiation with single beam of 1MeV electrons, 1MeV Ne^+, 1MeV Kr^+ and 1MeV Xe^+ induces amorphization in CuTi below the critical temperatures, 220K, 400K, 450K and 450K, respectively. Being consistent with these results, there are three temperature regions either of which shows characteristic microstructural changes in CuTi irradiated with 1MeV electrons and Kr^+ ions; (1) temperatures $T \leq 220K$ where both electrons and ions induce amorphization, (2) $220K \leq T \leq 450K$ where ions induce amorphization, nor do electrons and (3) $T \geq 450K$ where no microstructural changes occur.

Those studies give brief qualitative information on the synergistic effect of dual-beam irradiation. However, there have been neither systematic nor quantitative studies in this field. Systematic and/or quantitative studies on the dual-beam irradiation might provide insights not only into the mechanism of radiation damage itself but also into successful simulation of radiation damage of fission and fusion reactor materials.

1.3. OBJECTIVES OF THIS WORK

Four issues of fundamental importance are addressed in this thesis:

(1) Structure and accumulation of cascade damages in various non-metallic inorganic materials including ceramics and semiconductors

(2) Effects of concurrent irradiation with ions and electrons on the accumulation of cascade damages in Si and Ge

(3) Effects of concurrent irradiation with ions and electrons on irradiation-induced amorphization in Si

(4) Stability of cascade damages in Ge under electron irradiation and thermal annealing

HVEM has been successfully used for in-situ observation of the radiation damage by electrons because mainly of easy control of a wide variety of experimental parameters; e.g. electron energy, its dose rate, irradiation time, temperature and crystallographic orientation [13]. Fast electrons induce isolated point defects, so called Frenkel pairs, and evolve defect clusters through the nucleation and growth process. The possible use of HVEM-ACC facilities further provides in-situ observation under impulsive energy deposition, electronic excitation and ion irradiation. HVEM-ACC facilities were extensively used in this study. Then, theories on elementary processes of radiation damages especially on the primary process including irradiation induced phenomena will be reviewed in **chapter 2**. The detail description of experimental procedures together with the introduction of HVEM-ACC facilities will be appeared in **chapter 3**.

Accelerated ions induce cascade damages which are essential for fusion neutron irradiation damages. In order to clarify the characteristics of cascade damages in terms of characteristics of materials, 16 kinds of non-metallic inorganic crystals were irradiated with 30~60keV Ar^+ and Xe^+ ions. Experimental details and results will be shown in **chapter 4** together with the structure of cascade damages in Si and Ge.

The accumulation process of cascade damages will be investigated in **chapter 5**, especially at the early stage of ion irradiation (<10^{16} ions/m^2). Some of crystals being examined in **chapter 4** show up contrasts corresponding to cascade damages through transmission electron microscopy (TEM), which accumulate obeying a power low. The power represents the mechanism of showing-up contrasts of cascade damages. The accumulation of cascade damages will be affected by simultaneous electron irradiation which is essential for in-situ observation and for getting insights into the concurrent effect. The effect of concurrent irradiation with electrons on cascade accumulation will be studied in detail as functions of ion species, target element and electron dose rate. Kinetic equations which describe the synergistic effect will be proposed.

The ion-induced amorphization and the effect of concurrent irradiation with ions and electrons on the amorphization will be studied in **chapter 6**. Many of semiconductors [33-40] have been reported to be amorphized after high dose (≥10^{18}ions/m^2) irradiation with ions, so-called ion-induced amorphization. On the contrary, irradiation with fast electrons induces no amorphization in Si even after high dose irradiation at lower temperatures. The effect of cascade damages is thought to be essential for the ion-induced amorphization, because of the impossibility of electron-induced amorphization. The concurrent irradiation with ions and electrons on the ion-induced amorphization raises the author's scientific interest, because systematic studies with use of the concurrent irradiation will give us the successful understanding on the concurrent effect and further on the mechanism of the ion-induced amorphization.

The stability of cascade damages will be investigated in **chapter 7**. The concurrent effect on the accumulation process of cascade damages and on the ion-induced amorphization is dominated by stability of cascade damages. Therefore, studies on the stability of cascade damages are indispensable for discussing the concurrent effect. The stability of cascade damages will be investigated through the subsequent irradiation with electrons after ion irradiation and through the isochronal annealing of cascade damages.

The discussion on those four issues will give the quantitative understanding on cascade damages and the concurrent effect. Chapter 8 summarizes the results of this work together with future prospects on the simulation of neutron irradiation damage in terms of dual-beam irradiation with ions and electrons.

CHAPTER 2

FUNDAMENTALS OF IRRADIATION DAMAGE PROCESSES

When crystals are irradiated with energetic particles, the particles lose their kinetic energy along their trajectory through the atomic collision, electronic excitation, nuclear excitation, nuclear reaction and bremsstrahlung. The first two processes, which are called respectively nuclear and electronic energy loss processes, are important for describing the radiation damage process under irradiation with energetic particles having energy from keV to MeV. In the following sections, the energy loss and the damage processes, which will be used for analysis in the following chapters, are outlined briefly. The primary process of radiation damages is brought to a focus because of its primary importance in this thesis. Therefore, the radiation damage typical at very high dose region (~10^{20} particles/m^2), such as voids and bubbles will not be taken into account in the chapter.

2.1. THEORY OF ION-ATOM INTERACTION

The ion-atom interaction has been successfully described by Lindhard et al. [41-45], based on the Thomas-Fermi potential which includes interactions among nuclei and electrons. Their theory is a quasi-classical approximation giving fairly good description of the ion-atom interaction.

Suppose the energy transfer from a projectile (Z_1, M_1) with an incident energy E to a target atom (Z_2, M_2). The differential cross section of nuclear energy loss, $d\sigma_n$, is expressed by the following equation,

$$d\sigma_n = \pi a^2 \frac{dt}{2t^{3/2}} f(t^{1/2}) , \qquad (2.1)$$

where t is the dimensionless parameter of multiplication of incident energy E and transferred energy T, and is described as;

$$t = \varepsilon^2 \sin^2\frac{\theta}{2} = \varepsilon^2 \frac{T}{T_{max}}, \qquad (2.2)$$

$$\varepsilon = \frac{a}{Z_1 Z_2 e^2} \frac{M_2}{M_1+M_2} E \qquad (2.3)$$

and

$$T_{max} = \frac{4M_1M_2}{(M_1+M_2)^2} E . \qquad (2.4)$$

The Thomas-Fermi radius, a, is written as the following with the Bohr radius (a_0=0.529A),

$$a = \frac{1}{2}\left(\frac{3\pi}{4}\right)^{2/3} a_0 \left(Z_1^{2/3}+Z_2^{2/3}\right)^{-1/2} \qquad (2.5)$$

The values of $f(t^{1/2})$ are tabulated by Lindhard [44] and are given by the following Winterbon approximation [46];

$$f(t^{1/2}) = 1.309\, t^{1/6} [1+1.900\, t^{4/9}]^{-3/2}. \qquad (2.6)$$

Using eq.(2.1) to eq.(2.6), the universal function $f(t^{1/2})$ describes the scattering at all energies and scattering angles for all ion-atom pairs.

Since the stopping power is defined with the atom density N as follows,

$$S = N\int T d\sigma \quad , \tag{2.7}$$

eqs. (2.1) to (2.7) give the nuclear stopping power,

$$S_n = \frac{4M_1}{M_1+M_2} \pi a N Z_1 Z_2 e^2 \frac{1}{\varepsilon}\int_0^{\varepsilon} f(t^{1/2}) d(t^{1/2}) \quad . \tag{2.8}$$

One can rewrite eq. (2.8) in the following,

$$S_n = \frac{E}{\varepsilon}\frac{\rho}{z} s_n, \tag{2.9}$$

introducing a dimensionless quantity of length z which is defined as

$$\rho = z\,(4\pi N a^2)\,\frac{M_1 M_2}{(M_1+M_2)^2}, \tag{2.10}$$

and defining

$$s_n = \frac{1}{\varepsilon}\int_0^{\varepsilon} f(t^{1/2}) d(t^{1/2}) \quad . \tag{2.11}$$

The cross section of electronic stopping power is nearly proportional to the velocity of incident particles (v) for $v < v_0 Z_1^{2/3} = 2\pi e^2 Z_1^{2/3} / h = 2.19 \times 10^6 Z_1^{2/3}$m/s. The electronic stopping power in this velocity region is derived by Lindhard et al. [41-43] as,

$$S_e = N\xi_e\, 8\pi e^2 a_0 Z_1 Z_2 (Z_1^{2/3}+Z_2^{2/3})^{-3/2} \frac{v}{v_0} \tag{2.12}$$

and

$$\xi_e \approx Z_1^{1/6}.$$

Eq. (2.12) can be rewritten in a reduced unit, that is

$$s_e = k\,\varepsilon^{1/2} \qquad (2.13)$$

with

$$k = 0.0793\,\xi_e \frac{Z_1^{1/2}Z_2^{1/2}}{(Z_1^{2/3}+Z_2^{2/3})^{3/4}} \frac{(M_1+M_2)^{3/2}}{M_1^{3/2}M_2^{1/2}}, \qquad (2.14)$$

where M_1 and M_2 are in the unit of amu. Eq. (2.13) depends on ion-atom combinations, in contract to the universal eq. (2.11) for any combinations. **Figure 2.1** shows the reduced stopping power as a function of reduced energy $\varepsilon^{1/2}$. The value of s_n increases up to the maximum value with increasing the value of $\varepsilon^{1/2}$ and then decreases, while that of s_e is proportional to $\varepsilon^{1/2}$.

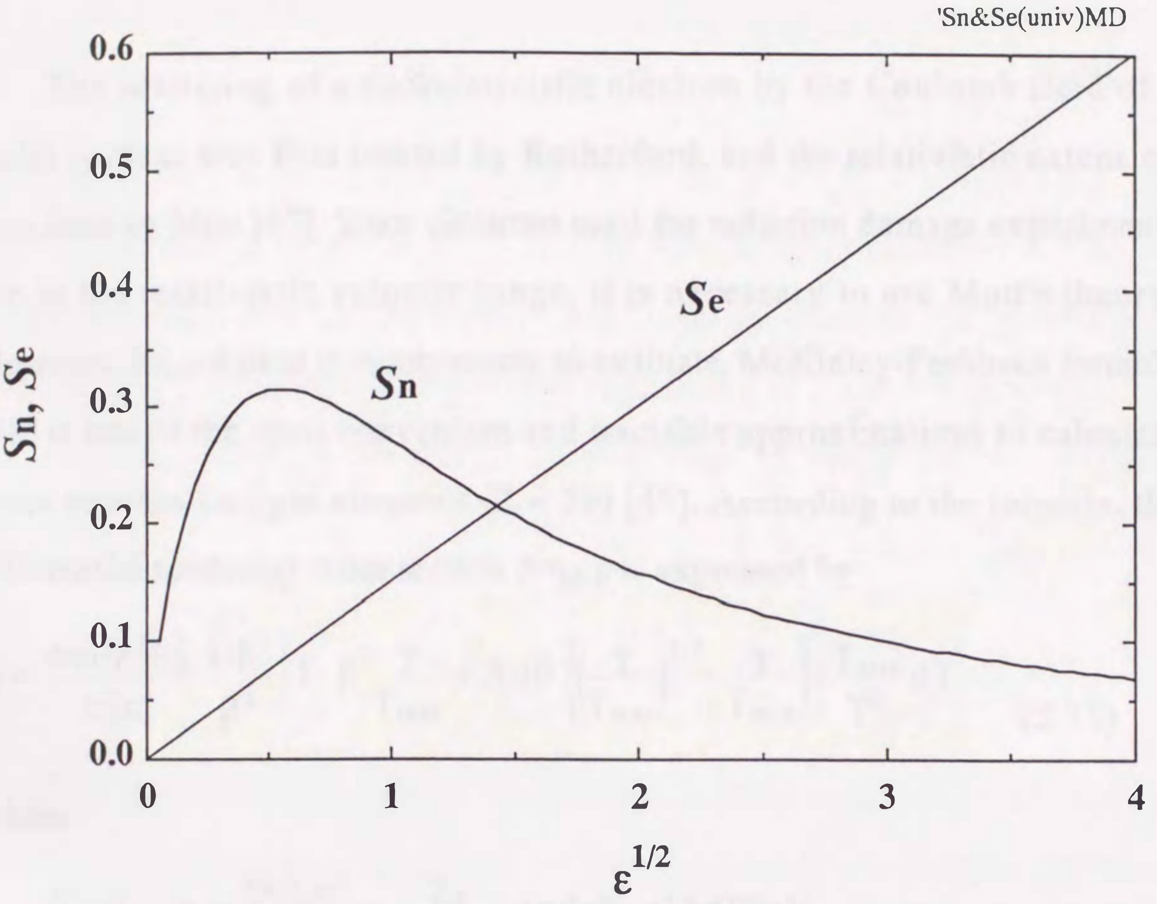

Figure 2.1 Reduced nuclear and electronic stopping powers, S_n and S_e, as a function of reduced energy, ε. The value of $\varepsilon^{1/2}$ is proportional to the velocity of incident particles.

2.2 THEORY OF ELECTRON-ATOM INTERACTION

The scattering of a nonrelativistic electron by the Coulomb field of a point nucleus was first treated by Rutherford, and the relativistic extension was done by Mott [47]. Since electrons used for radiation damage experiments are in the relativistic velocity range, it is necessary to use Mott's theory. However, his solution is cumbersome to evaluate. McKinley-Feshbach formula [48] is one of the most convenient and tractable approximations to calculate cross sections for light elements (Z < 29) [49]. According to the formula, the differential scattering cross section $d\sigma_{M-F}$ is expressed by

$$d\sigma_{M-F} = \frac{4\pi a^2 Z_2^2 E_R^2}{m_e^2 c^4} \frac{1-\beta^2}{\beta^4} \left[1 - \beta^2 \frac{T}{T_{max}} + \pi\alpha\beta \left\{ \left(\frac{T}{T_{max}} \right)^{1/2} - \frac{T}{T_{max}} \right\} \right] \frac{T_{max}}{T^2} dT , \qquad (2.15)$$

where

$$\beta = \frac{v}{c}, \quad \alpha = \frac{2\pi Z_2 e^2}{h c} = \frac{Z_2}{137.04} \text{ and } E_R = 13.605 \text{eV} .$$

T_{max} is the maximum transferred energy, and it is given by

$$T_{max} = 2E\left(E + 2m_e c^2\right) / M_2 c^2. \qquad (2.16)$$

The nuclear stopping power is, therefore,

$$S_n = N \int_{T_{mim}}^{T_{max}} T \, d\sigma$$

$$= \frac{4\pi a_0^2 Z_2^2 E_R^2}{m_e^2 c^4} \frac{1-\beta^2}{\beta^4}$$
$$\times \left[T_{max} \ln\frac{T_{max}}{T_{min}} + 2\pi\alpha\beta T_{max}^{1/2}\left(T_{max}^{1/2} - T_{min}^{1/2}\right) - \left(\beta^2 + \alpha\beta\right)\left(T_{max} - T_{min}\right) \right]. \tag{2.17}$$

The lower limit of the integration depends on the property of interest, e.g. the appropriate energy of the lower limit is the displacement threshold energy E_d for atomic displacements, whereas it is the migration energy of vacancies or interstitials for the irradiation induced migration [50]. The total cross section for producing atomic displacements by an electron of energy E can be written as

$$\sigma_{tot}(E,E_d) = \int_{E_d}^{T_{max}} \nu(T) \frac{d\sigma}{dT} dT \quad , \tag{2.18}$$

where $\nu(T)$ is the average number of displacements and called the damage function. For the electron energy about 1MeV, which is our interest, electrons produce isolated Frenkel pairs. Values of σ_{tot} are tabulated by Oen [49] for 37 different elements as a function of electron energy using several different threshold energies.

The electronic stopping power for a relativistic electron is given by Bethe [51], that is

$$S_e = \frac{4\pi e^4}{m_e v^2} N Z_2$$
$$\times \left[\ln\left(\frac{m_e v^2 E}{2\, I^2}\right) + \ln\frac{1}{1-\beta^2} - \left\{2\left(1-\beta^2\right)^{1/2} - 1 + \beta^2\right\} \ln 2 + 1 - \beta^2 + \frac{1}{8}\left\{1 - \left(1-\beta^2\right)^{1/2}\right\}^2 \right], \tag{2.19}$$

where m_e and v are the rest mass and the velocity of electrons, respectively. I is the ionization energy and is described in the unit of eV as

$$I \approx 9.73\, Z_2. \tag{2.20}$$

2.3. DAMAGE PRODUCTION

The PKA energy (T) ranges from zero to its maximum value (T_{max}) which depends on the combinations of projectiles and targets. The number of displaced atoms is proportional to T below about A keV (the mass number of target atoms) and it levels off for higher values of T where the major part of the energy is lost through the electronic energy loss process [52]. The transferred energy less than E_d is mainly dissipated into phonon excitation (lattice vibration). These damage production processes will be reviewed briefly in the following sections.

2.3.1. POINT DEFECT PRODUCTION

When the PKA energy is nearly equal to E_d, PKAs are displaced from their original sites to form isolated Frenkel pairs. Electron irradiation, therefore, induces mostly isolated Frenkel pairs, and some of them aggregate to form interstitial or vacancy clusters through the nucleation and growth process. High voltage electron microscopy (HVEM) has been used for in-situ observation of the nucleation and growth process of defect clusters or dislocation loops. The loop formation during fast electron irradiation was first observed in late '60s in Ni [53], Au [54] and a simple theory for describing the process was presented by Makin [55]. Since then, plenty of information on point defects (e.g. migration energy and their kinetics) and defect clusters (e.g. habit plane and Burgers vector of loops) have been derived in metals [56], semiconductors [57] and in ceramics [58-60]. The migration energy of point defects is derived from the temperature dependence of defect clusters and/or the growth and the shrinkage behavior of defect clusters during electron irradiation. Values of the migration energy of point defects are quite consistent with theoretical prediction except for materials in which the behavior of point defects is expected to be complicated like in silicon. The nature of loops such as the Burgers vector and habit planes are derived from TEM using **g·b** analysis, inside-outside technique, trace analysis [61] and 2-1/2-D method [62]. Examples are unfaulted interstitial loops with b=1/2<110> on {113} planes in electron irradiated Si and Ge [63], pure edge dislocation loops of interstitial character with b=1/3[0001] on the basal plane and b=1/3$[10\underline{1}0]$ on the prismatic $\{10\underline{1}0\}$ planes in alumina [65,66] and perfect 1/2<110>{110} interstitial edge dislocation loops with elongation mode along <001> [60]. Characterization of interstitial loops in $MgAl_2O_4$ irradiated with fission neutrons has been investigated by Nakai et al. [66].

2.3.2. CASCADE PRODUCTION

The linear Boltzman transport equation [41-46,67-70], in which small collision density, simple interatomic potentials and disregard of the crystal structures are assumed, gives the number of recoil atoms increasing linearly with the nuclear energy loss. However, as increasing nuclear energy, the higher density of recoil energy is deposited within the smaller volume. In this condition, a violently disordered region, whose volume depends on projectiles and target atoms, will be created [71]. Such phenomena are generally termed 'spikes' or 'energy spikes.' The energy, which is very much higher than the thermal energy, is deposited within 10^{-13} to 10^{-12} s [72-74] and dissipates into the surrounding lattice. It results in non-linear effects on sputtering yields [75,76] and on the number of defect production.

A spike is generally described in two ways [77], one is in terms of the energy of atoms in the spike and the other is of the density of point defects.

(1) A spike region is a local volume in which essentially all the atoms are instantaneously in 'motion.' The definition of the motion is nebulous since it must be specified in terms of some minimum energy. Heat of melting and the sublimation energy are taken as upper limits of the energy for radiation damage and sputtering, respectively.

(2) A spike region is a local volume in which the defect density exceeds some critical value such that the lattice undergoes a major rearrangement to accommodate these defects; e.g. a crystalline to amorphous transition.

So far, four kinds of spike phenomena have been proposed, i.e. the displacement spike, thermal spike, plasticity spike and ionization spike. First three kinds of spike phenomena will be briefly described in the following and the last one will be done in the next section.

The concept of the 'displacement spike' has been proposed by Brinkman [78,79]. Incident particles transfer their energy to PKAs. PKAs generate sequences of collisions within $10^{-13} \sim 10^{-12}$ s. The mean free path between atomic collisions becomes smaller as PKAs and the subsequent displaced atoms lose their energy through collisions, and finally it approaches the interatomic spacing. As a result, vacancy-rich regions surrounded by interstitial atoms are formed. Those are displacement spikes. In case of irradiation with fast neutrons or heavy ions, a cascade damage consists of several diluted regions surrounded by interstitial atoms, each of which is called 'subcascade'. The average energy of point defects is high enough to produce other displacements in the displacement spike.

At the final process of the propagation of the displacement spike, however, the average energy of atoms in the spike reaches below E_d and the region alters for 'thermal spike' [80]. The thermal spike is the result of the transfer of a large amount of kinetic energy from the incident projectile to lattice atoms within a small volume of materials. The deposited energy is not enough for direct atomic displacements, but it is converted to the vibrational or electronic excitation energy through the electron-phonon interaction or the non-radiative transition [81,82]. The temperature in a thermal spike volume is theoretically estimated to surpass the melting point of solids (~eV), over a sufficiently long time (~10^{-11} s) to render the liquid structure. The region is, therefore, conceived as representing a superheated solid. In the context of high density cascades which are described as quite large energy density (~2eV) within each cascade region, the density of recoil is very high such that many atoms dispersed over the cascade volume are simultaneously in this energy sharing the state with neighboring atoms.

Spike phenomena play important roles for the structure and the stability of cascade damages particularly produced by the high energy PKA in semiconductors [71,83,84]. Various investigations on Si and Ge using ion-backscattering channeling technique [85-87] or TEM [88-90] have shown that collisional cascade theories [67,70,91] appreciably underestimate the number of displaced atoms whenever the average deposited energy density in a cascade damage $<\theta_v>$ is larger than a few tenths of eV/atom. The parameter $<\theta_v>$ is defined as the average of nuclear energy deposition per an atom within an individual cascade region. In the case that $<\theta_V>$ is larger than 2 eV/atom, a very large fraction of the volume of collision cascades theoretically predicted is rendered as amorphous [88-90,92,93]. When $<\theta_V>$ is less than 0.5 eV/atom, there are localized regions (i.e. subcascades) which are essentially amorphous, but they are obviously surrounded by areas having a high density of point defects and small defect clusters.

The energy deposition causes the outward motion of atoms from the center of cascade damages and produces a local transient pressure. The pressure may compress the surrounding medium and establish 'plasticity spike' or 'shock wave.' Guinan [94] has estimated the effect of the shock wave and concluded that the shock wave is generated by the 10~100keV cascade damages within ~10^{-12} s. A cascade damage having $<\theta_V>$ of 1 eV/atom was estimated to generate the shock wave with 1 GPa [77], which was several orders of magnitude in excess of metallic elastic limits. The shock wave may cause surface spalling [94], which can be described as the separation of material under dynamic tensile loading. At lower temperatures where vacancies are immobile, the cascade core might be an invisible vacancy cluster through TEM. The shock wave could rearrange vacancies within cascade regions to form visible clusters. Kiritani et al. [95] have observed the microstructural evolution in neutron irradiated Cu, Ni and Au, and have estimated the diameter of the volume influenced by the shock wave to be 110nm for Cu and Au.

2.3.3. ELECTRONIC EXCITATION

Fast ions mainly lose their kinetic energy through the interaction with electrons in solids. Very high energy particles of the order of 100MeV are considered to strike or carry electrons with the particle [96], and the low energy ones of the order of keV~MeV excite electrons to the Fermi level [42,97]. It is quite reasonable to regard that the effect of electronic excitation depends on the kind of chemical bonding.

In metals, these interactions are negligible at higher temperatures, because phonon energy is larger than that transferred from excited electrons to phonons through the electron-phonon interaction. At low temperatures, however, the energy can contribute to the annihilation of pre-doped isolated Frenkel-pairs [98-101] and cascade damages [102,103], called irradiation annealing, and it also contributes to the production of isolated Frenkel-pairs [99,100].

In alkali halides, X-ray irradiation produces neutral vacancies (F-centers) and interstitials (H-centers) through the non-radiative transition process [81,82], making halide molecule ions [104] along <110> directions due to effective energy transfer from an exciton to a halide molecule ion. In dielectric materials, highly energetic heavy ions introduce nuclear tracks with energy deposition density more than 1000 eV/A. Such tracks have been applied in an astonishing variety of fields including the earth and planetary sciences, chemistry, nuclear engineering and others [105].

Many studies have been done on nuclear tracks in platinum phthalocyanine [106], yttrium iron garnet [107-110], UO_2 [111] and zircon

($ZrSiO_4$) [112,113]. Smaller thermal diffusivity is considered to cause the nuclear track formation. The thermal spike model [105] and the ion explosion model [105] are proposed for the formation. In the former model, the ionization creates a narrow intensely 'hot' region where most of all atoms move around like liquid state and the subsequent quenching to a disordered or amorphous state. In the latter one, the ionization creates a core of positive ions whose mutual repulsion leads to a dense array of interstitial and vacant lattice sites, and subsequent relaxation produces long range strain fields which have been observed by TEM [106,110,111]. High resolution electron microscopy (HREM) has been also used for observation of disordered and amorphized regions along the track [110,112,113].

2.3.4. IRRADIATION INDUCED DIFFUSION OF POINT DEFECTS

When the lattice vibration of an atom around a vacancy is excited more than the activation energy for the vacancy migration E_m^v, the atom is thought to be displaced from its original position to the vacancy position and has a similar effect to the thermal migration of vacancies [51]. The same phenomenon is expected to happen for atoms at the interstitial position. Those phenomena are called irradiation-induced diffusion.

CHAPTER 3

EXPERIMENTAL PROCEDURES

3.1. APPARATUS

3.1.1. HVEM-Accelerator facility at Kyushu University (KU)

Figure 3.1 schematically shows horizontal and vertical views of the HVEM-ACC facility at KU which is comprised of a 1250kV HVEM (JEM1000), an ion accelerator (Origin Electric Co.Ltd.) and an imaging system. The ion accelerator consists of a duo-plasmatron ion source, an accelerating unit having the maximum voltage of 30kV, two electromagnetic lenses (Lens 1 and 2), a mass-analyzing magnet deflecting 15 degrees and an electrostatic prism. Two gate valves separate the ion accelerator into three parts, the lowest stream of which is involved in HVEM. Each of other two parts is connected with a diffusion pump with a cold trap, as shown in **figure 3.1**.

Figure 3.2 schematically shows a vertical cross section of the accelerator. The duo-plasmatron ion source is composed of a gas leak valve, a vortex filament, an arc wenelt and a magnet. Emitted electrons from the filament whose energy is about 10-100 eV move spirally in a dilute gas of $5x10^{-5}$ torr making charged gas. The charged gas is, then, accelerated up to the maximum voltage of 30kV. Ion beams are focussed or defocussed by two lenses (Lens1 and 2) and are mass- and energy-analyzed by the analyzing

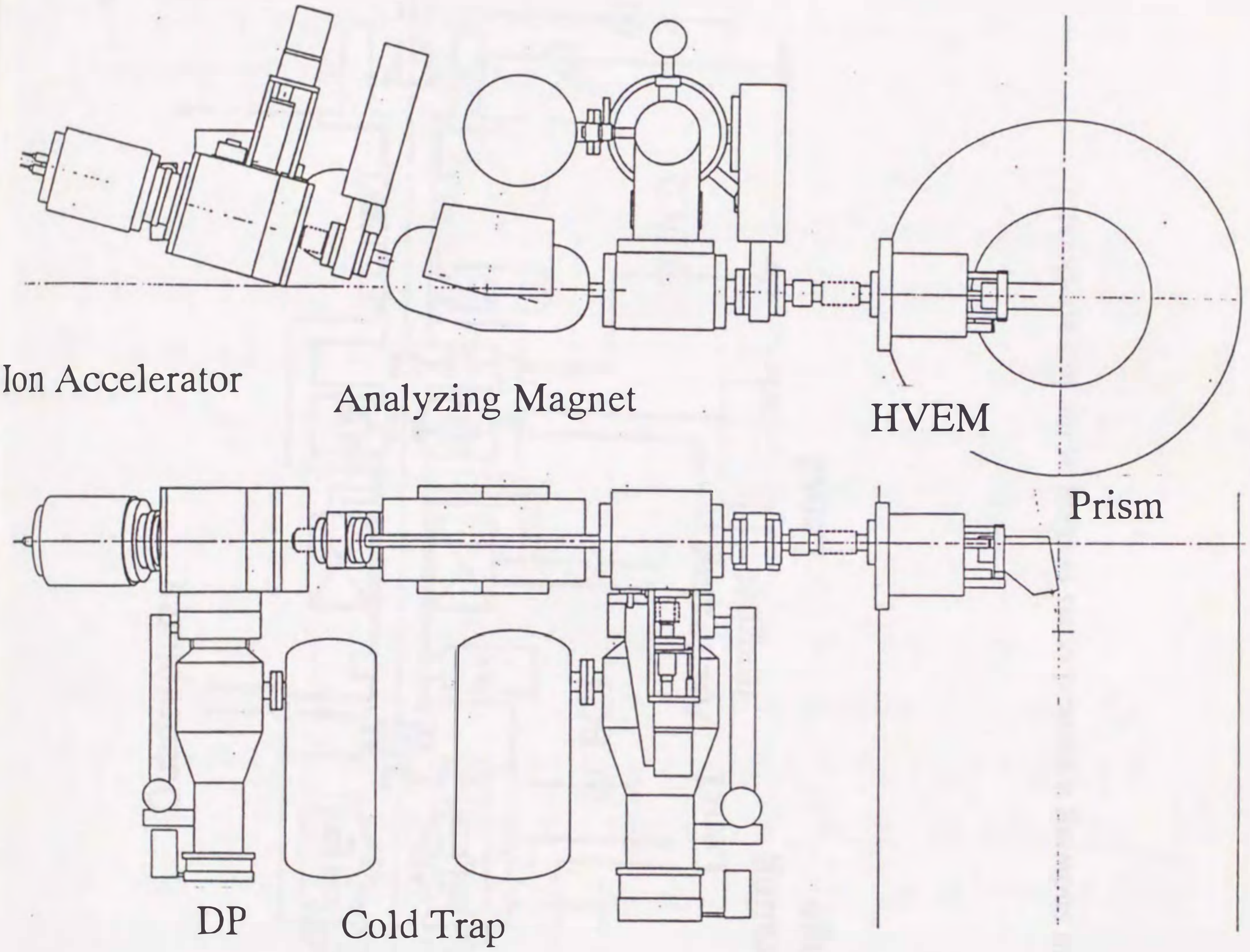

Figure 3.1 A schematic diagram showing horizontal and vertical views of the HVEM-ACC facility at KU, which consists of an HVEM, an ion accelerator and an imaging system.

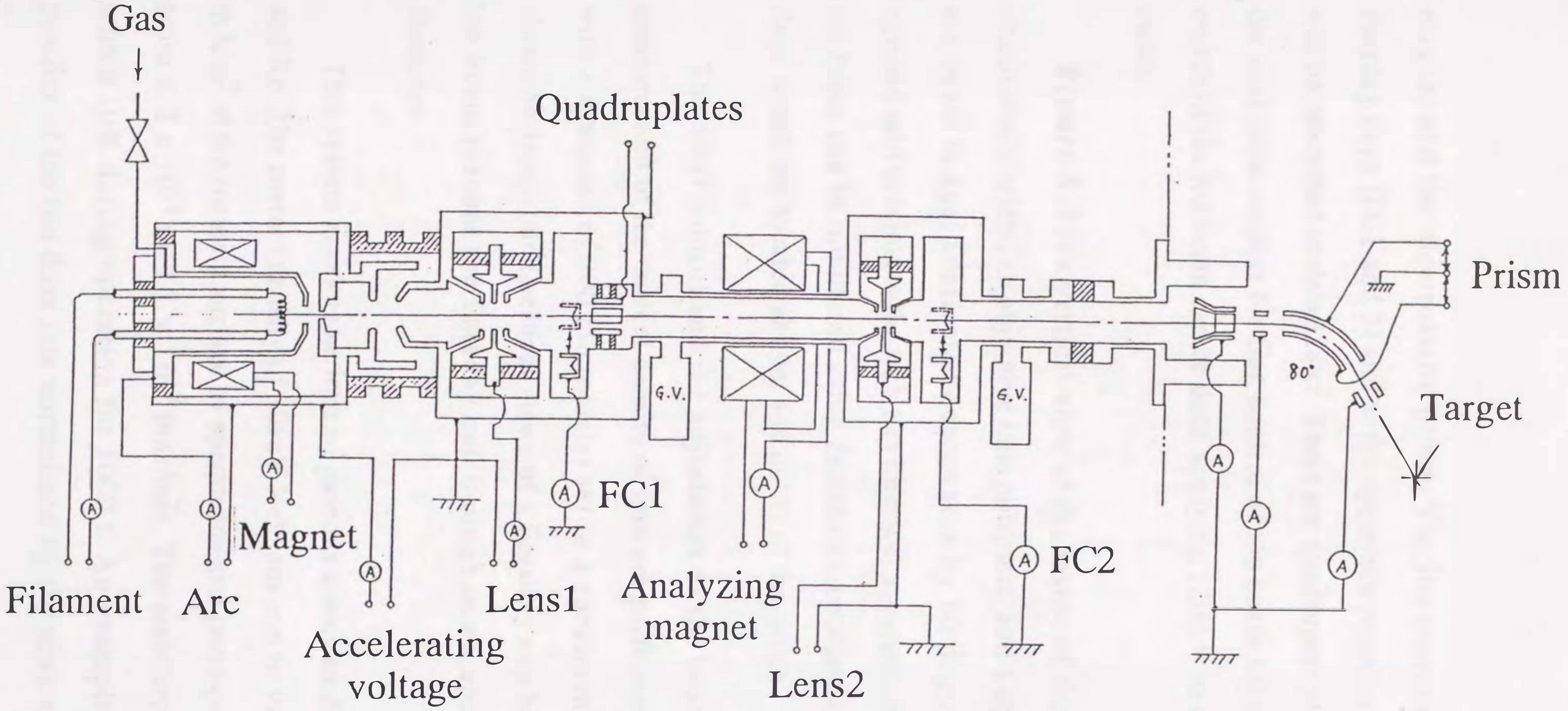

Figure 3.2 A schematic diagram showing a vertical cross section of the ion accelerator.

magnet and the electrostatic prism. The ion current is measured at two Faraday cups (FC1 and 2) and at the specimen position in the HVEM, which will be described in detail later. There are quadrupole plates between FC1 and the analyzing magnet for fine control of ion beam adjustment. The electrical switch of the ion beam can be done applying 1200 V to one of the quadrupole plates.

Figure 3.3 is a vertical view of the inside of the HVEM showing the electrostatic prism, an objective lens polepiece and a specimen position. The ion beam is again deflected downwards by 80 degrees by the prism and injected into specimens through a cylindrical aperture of 2 mm diameter. The ion beam can be monitored using detectors comprised of four plates and two rings which are located at inlet and outlet of the prism.

The final control and the adjustment of the beam line as well as the measurement of the current density of ions are performed using a Faraday cup with a diameter of 200 micrometer set in a specimen holder. **Figure 3.4** shows horizontal and vertical views of a Faraday cup holder (SFH100). The ion beam reaches the Faraday cup through as an aperture of 0.2 mm in diameter.

This system accelerates ions of gaseous atoms such as H, He, Ne, Ar, Kr and Xe. The current density of 30keV Xe^+ ions can be varied from 0.01 to 50 mA/m^2 at the incident surface of specimens and corresponds to ion dose rates from 6.2×10^{14} to 3.1×10^{17} $ions/m^2s$. The stability of the ion current is within 10% during operation for 1000 s. An example of two dimensional profiles of the ion dose rate normalized by the peak value on the specimen

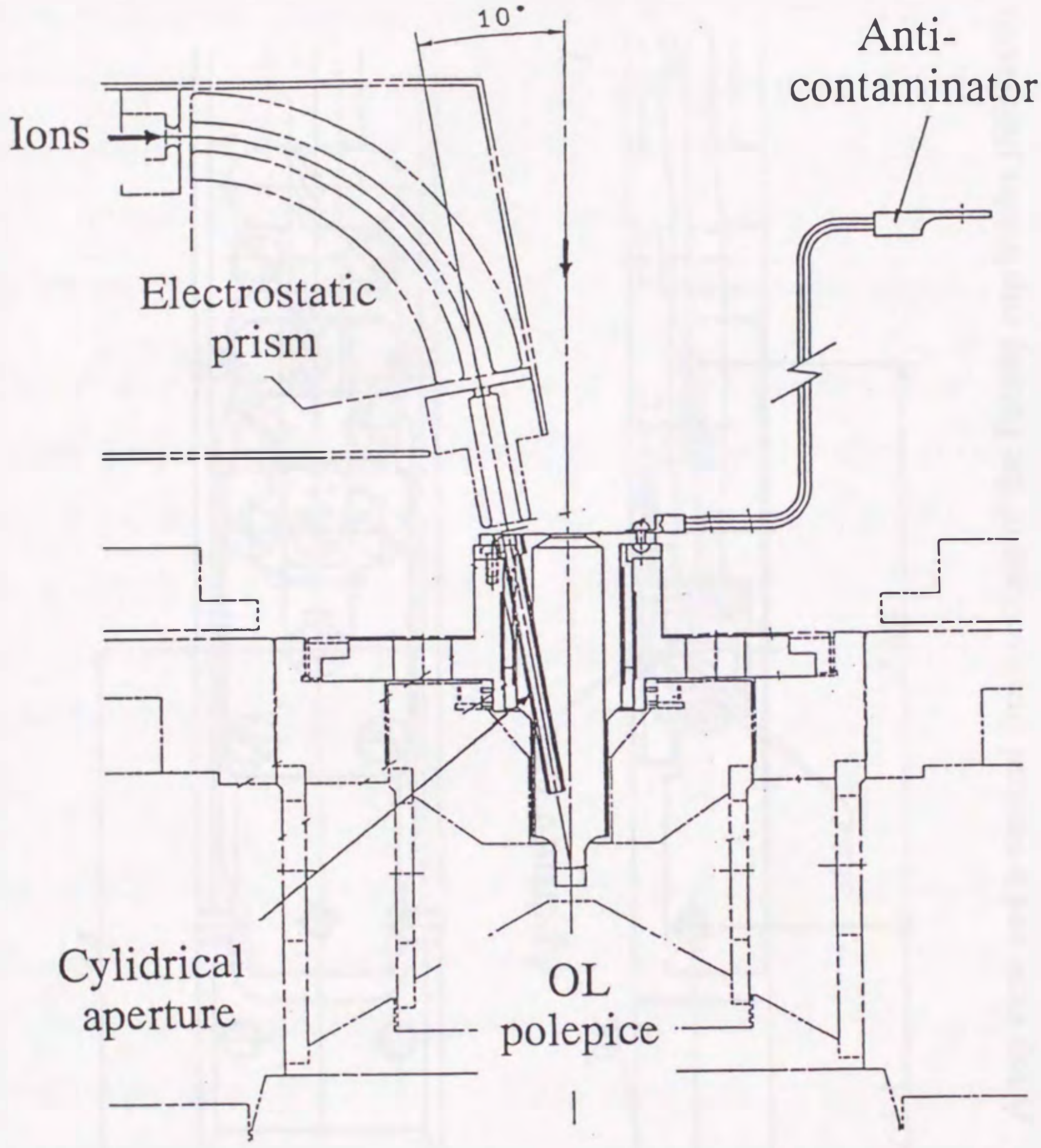

Figure 3.3 A schematic diagram showing a vertical view of the inside of the HVEM.

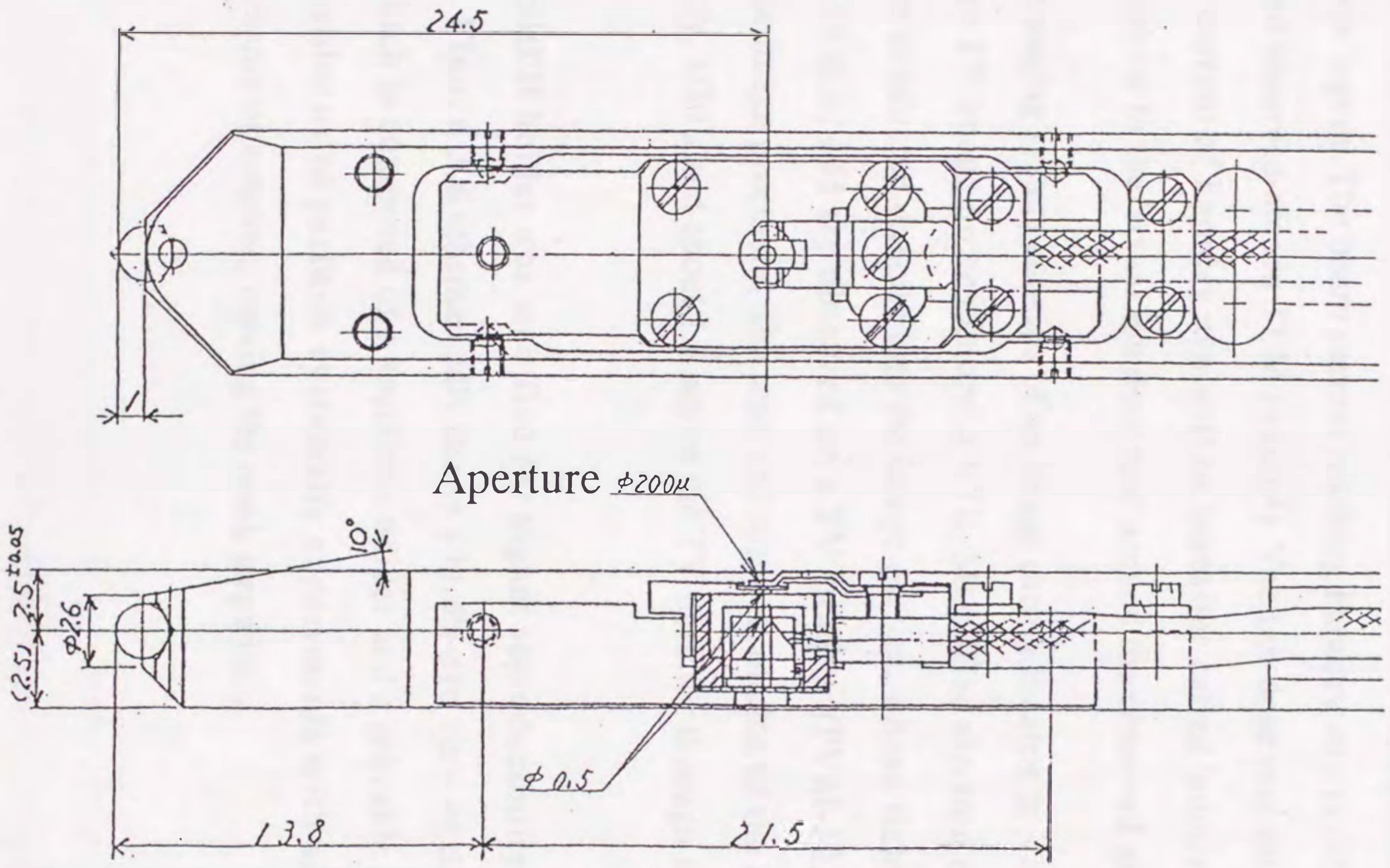

Figure 3.4 A top view and a vertical cross section of the Farady cup holder (SFH100).

surface is shown in **figure 3.5**. The ion dose rate along the Y-axis is rather uniform, but that along the X-axis is still nonuniform due to astigmatism of the electrostatic prism. However, observations were always performed within the uniform region. The beam current reaching Faraday cup is different from that around observed area in TEM ($\sim 1\mu m^2$). The ion dose rate obtained from the beam current of Faraday cup will be hereafter called 'nominal ion dose rate' in contrast to the 'actual ion dose rate' around the observed area.

The imaging system consists of an image carrier located in a camera box, a real-time TV image processor and a VTR. Magnified electron microscopic images are conducted directly into the image carrier, whose field of view is 13mm x 10 mm, and are observed on a TV monitor (PVM-122J, SONY) through the image processor. The time and space resolution of the images are, respectively, 1/30 s and about 1.5 nm on the TV monitor through the imaging system.

The SHEH holder was modified for higher reproducibility and easier operation. **Figure 3.6** schematically shows a bird's-eye view of the modified SHEH, which is composed of a specimen holder and a movable mask. This holder enables us to perform systematic experiments with an identical crystallographic orientation, moving the mask stepwisely.

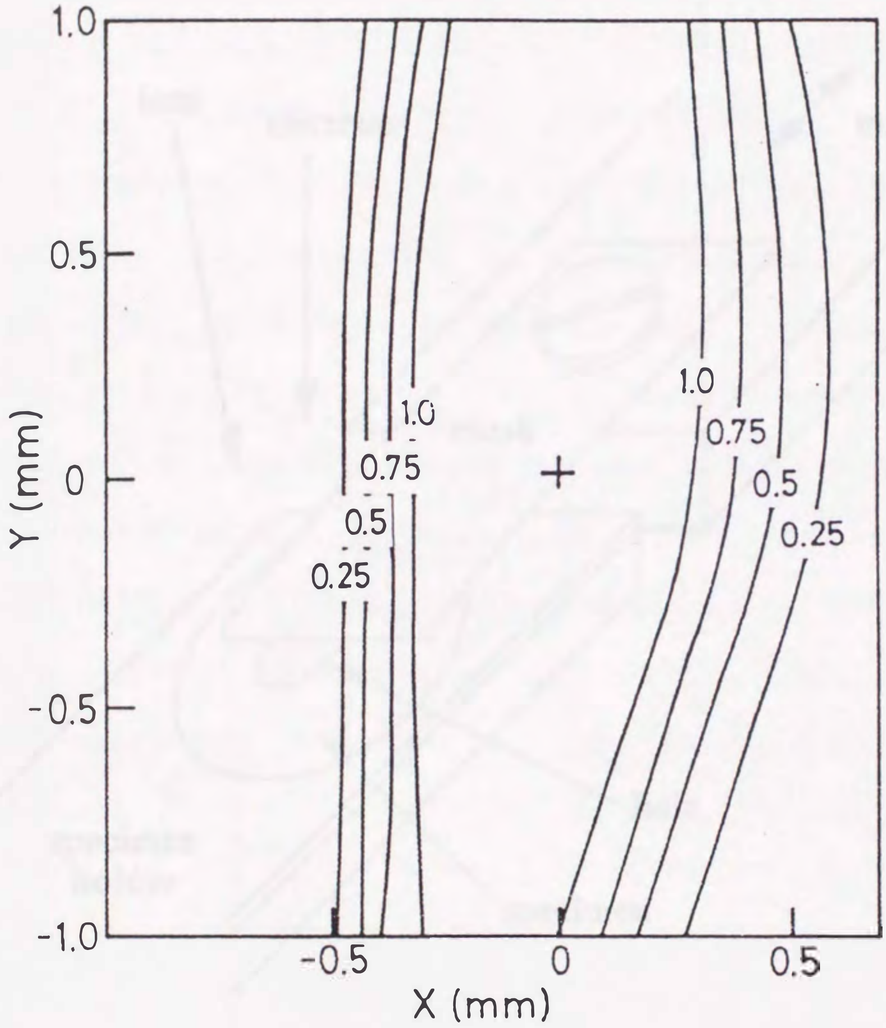

Figure 3.5 A typical example of two-dimensional profile of the 30keV Xe^+ ion dose rate normalized by the peak value on the specimen surface. The mark + shows the position of the electron beam under the in-situ observation.

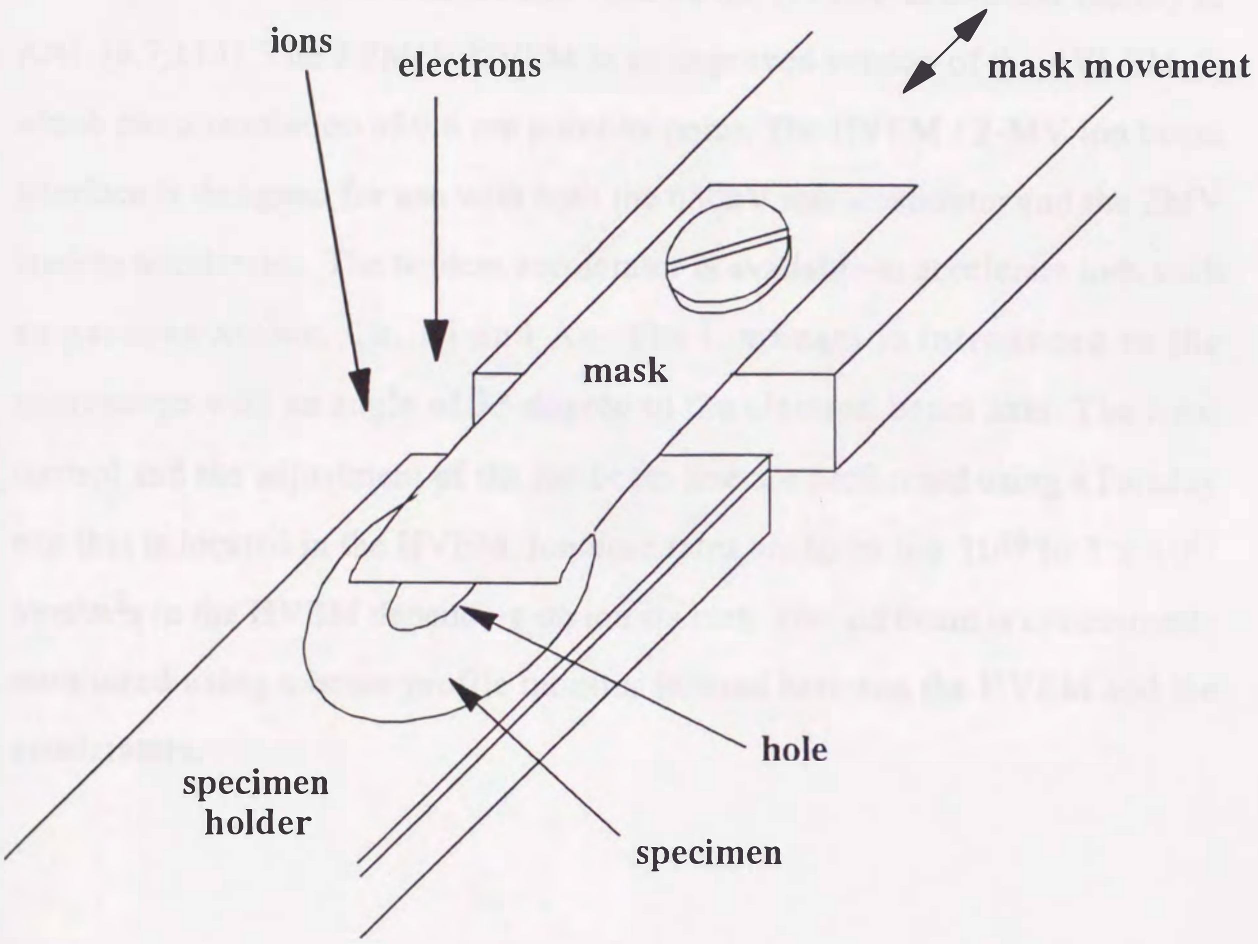

Figure 3.6 A schematic bird's-eye view of the modified elongation holder (SHEH).

3.1.2. HVEM-TANDEM FACILITY AT ARGONNE NATIONAL LABORATORY (ANL)

Figure 3.7 shows a bird's-eye view of the HVEM-TANDEM facility at ANL [6,7,114]. The 1.2MeV HVEM is an improved version of the AEI EM-7, which has a resolution of 0.6 nm point-to-point. The HVEM / 2-MV ion beam interface is designed for use with both the 650kV ion accelerator and the 2MV tandem accelerator. The tandem accelerator is available to accelerate ions such as gaseous atoms, Cu, Ni and Au. The ion beam is introduced to the microscope with an angle of 33 degree to the electron beam axis. The final control and the adjustment of the ion beam line are performed using a Faraday cup that is located in the HVEM. Ion dose rates are from 6 x 10^{14} to 1 x 10^{17} ions/m^2s in the HVEM depending on ion species. The ion beam is concurrently monitored using a beam profile monitor located between the HVEM and the accelerators.

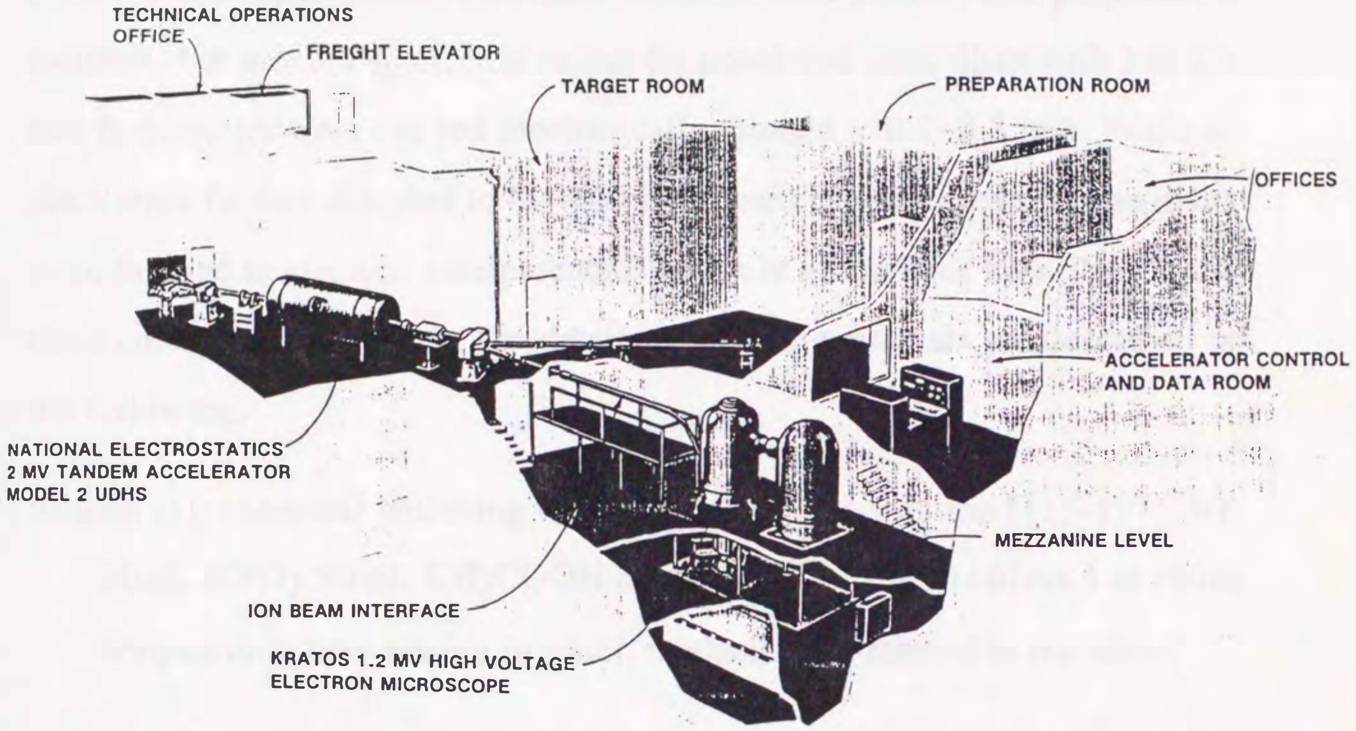

Figure 3.7 A bird's-eye view of ion accelerators at the HVEM-Tandem Facility of the HVEM and the ion accelerators.

3.2. SPECIMEN PREPARATIONS

Various kinds of ceramics and semiconductors listed in **table 3.1** were used for the experiments. The table includes their sources and preparation methods. For most of specimens except for powdered ones, disks with 3 or 2.3 mm in diameter were cut and mechanically thinned to 0.2~0.3 mm. Some of them were further dimpled to 80~100 micrometer in thickness. Those disks were thinned to electron transparencies with use of methods described in the third column of **table 3.1**. The details of thinning methods are described in the following;

Silicon (1): chemical polishing with solution (CP-4 solution [115-117]; HF 30ml, HNO_3 50ml, CH_3COOH 30ml and Br_2 few droplets) at room temperature, then rinsing in water, methanol and ethanol in the order,

Silicon (2): chemical polishing with solution (HF 125ml, HNO_3 325ml and H_3PO_4 50ml) at 250K, then rinsing in CH_3COOH at first, methanol and ethanol in the order [118],

Germanium (1): chemical polishing with CP-4 solution at room temperature, then rinsing in water, methanol and ethanol in the order,

Germanium (2): electrical polishing with solution (H_2SO_4 90ml, HF 30ml and methanol 500ml) at 210K with voltage of 70V [118],

MgO: chemical polishing with H_3PO_4 solution at 400K, then rinsing in distilled water for several seconds at room temperature [119],

Al_2O_3: ion thinning with 6 or 7keV Ar^+ ions, then annealing at 1673K in air for 1 hour to get rid of ion-induced damage [120],

$MgAl_2O_4$: ion milling with 6 or 7keV Ar^+ ions,

Other ceramics: crushing in an alumina mortar into fragments for electron transparency and dispersing into n-propyl alcohol.

Table 3.1. A list of samples, sources and preparation methods for TEM specimens

Sample	Source	Preparation method
Si	Komatsu Elec.	Chemical polishing or Crushing
Si	Kyushu Elec.	Chemical polishing
Si	Virginia Semicond. Inc.	Chemical polishing
Ge	Sumutomo Met. Min.	Chemical polishing or Electrical polishing
Ge-20at.% Si	Si:Kyushu Elec. Ge:Sumutomo Met. Min.	Crushing
Ge-33at.% Si	Si:Kyushu Elec. Ge:Sumutomo Met. Min.	Crushing
Graphite	Union Carbide	Cleaving
SiC	Taiheyo Carborundum	Ion milling or Crushing
WC	Japan New Met.	Crushing
VC	Japan New Met.	Crushing
TaC	H. C. Stark	Ion milling
TiC	Tateho Chem.	Electrical polishing or Crushing
HfC	H. C. Stark	Ion milling
Al_2O_3	Linde	Ion milling and annealing
ZrO_2	Shinko	Ion milling
$MgAl_2O_4$	Linde	Ion milling
MgO	Tateho Chem.	Chemical polishing or Ion milling

CHAPTER 4

MICROSTRUCTURAL EVOLUTION OF CASCADE DAMAGES

4.1. INTRODUCTION

Energetic ions make series of collisions and generate cascade damages in materials. The structure of cascade damages, e.g., the size of cascade damages and the concentration and distribution of point defects, in non-metallic inorganic crystals might be characterized in terms of the energy density within each of cascades and by the atomic bonding. Non-metallic inorganic crystals, especially candidate materials for fusion reactors, consist of low-Z elements. In low-Z materials, the portion of high energy PKAs is larger than in high-Z ones. High energy PKAs generate cascade damages with relatively longer mean free paths of the collisional events, i.e., dilute concentration of point defects. As a result, the lower energy density cascades is introduced. In high energy density cascades, on the contrary, vacancies or interstitials produced within cascade damages agglomerate and collapse into defect clusters, or phase transition readily occurs in the cascade regions. The kind of atomic bonding of non-metallic inorganic materials is described in terms of ionicity [124]. Ionic crystals, such as NaCl and MgO, have larger spontaneous recombination volume of point defects [125] because of the long range Coulomb interaction. In covalent crystals, such as Si and Ge, atoms within cascades are in motion during thermal spike phase [77] with energy far higher than melting point.

The subsequent quenching leaves amorphous regions within the cascade regions [88-93,121-123].

Transmission electron microscopy (TEM) detects microstructural evolution, such as cascade damages themselves, defect clusters and phase transitions, through diffraction contrast or strain contrast. Therefore, the probability for a single ion to produce a visible contrast in TEM is a good measure for the cascade structure and its stability. The HVEM-ACC facility together with the VTR recording system provides in-situ observation of the accumulation process of cascade damages at early stage of irradiation.

The objectives in this chapter lie in (1) clarifying the structure of cascade damages in various kinds of non-metallic inorganic crystals and (2) predicting which crystals enhance the contrast corresponding to cascade damages in TEM.

4.2. EXPERIMENTAL PROCEDURES

Sixteen kinds of non-metallic inorganic crystals were prepared for TEM transparencies and irradiated with 30keV Xe^+ ions and 250keV or 1MeV electrons at room temperature in the HVEM-ACC facility at KU. Powder specimens of Si, Ge, Ge-20at.% Si and Ge-33at.% Si were also irradiated with 40 and 60keV Nb^+ ions in an ion accelerator at the Research Reactor Institute, Kyoto University, and they were examined by TEM.

4.3. RESULTS AND DISCUSSION

Tiny defect clusters were observed in Si, Ge, Ge-20at.% Si, Ge-33at.% Si and GaAs irradiated with 30keV Xe^+ ions, and they increased in their number within a few seconds. The micrographs in **figure 4.1** are typical examples of weak-beam dark-field (WB) images showing tiny defect clusters induced in Si and Ge under dual beam irradiation with 30keV Xe^+ ions and 250keV or 1MeV electrons. Most of these contrasts are attributable to be amorphous [88-93,121-123] which is essentially corresponding to cascade damages, and will be called cascade contrasts in this literature. On the contrary, in non-metallic inorganic specimens other than Si, Ge, Ge-20at.% Si and Ge-33at.% Si, no cascade contrasts appeared in the early stage of irradiation. Further irradiation induced amorphous phase or dot contrasts after irradiation to higher dose levels. **Figure 4.2** shows examples of dot contrasts appeared in (a) MgO and (b) $MgAl_2O_4$. The microstructure corresponding to dot contrasts has not been identified, but is presumably attributable to interstitial dislocation loops (I-loops) [120].

The microstructural evolution of cascade damages depends strongly on the spatial distribution of point defects in individual cascade damages. The area density of individual contrasts, N, in various specimens was examined during dual-beam irradiation with 30keV Xe^+ ions and 250keV or 1MeV electrons. Typical examples of experimental results are shown in **figure 4.3**, where N/P, P being the ion dose rate, is plotted as a function of irradiation time. The area density, N, which depends scarcely on the specimen thickness,

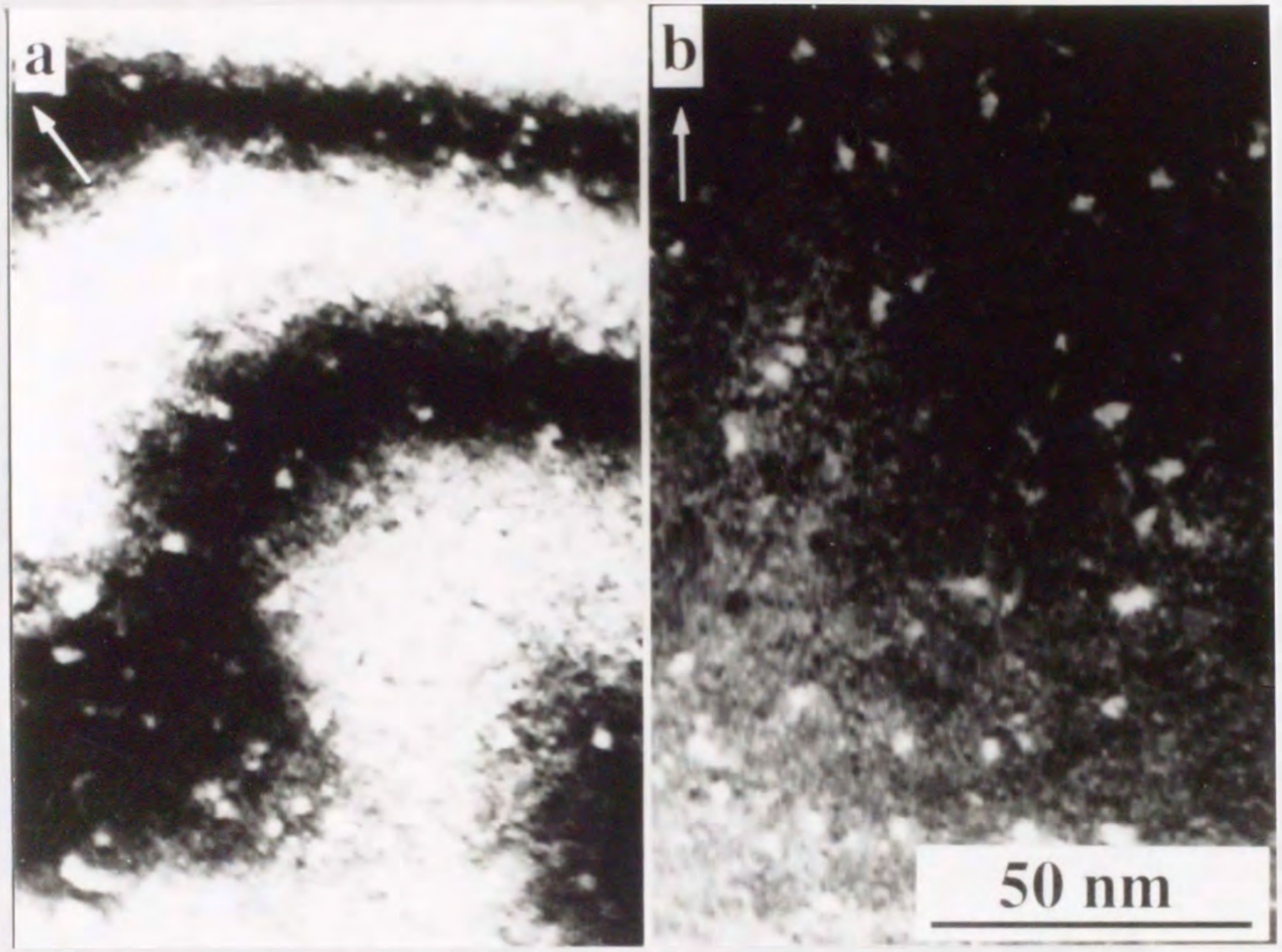

Figure 4.1 Weak-beam dark-field images on TV monitor through the imaging system, showing cascade contrasts in (a) Si irradiated with a 30keV Xe^+ ion dose rate of $2.5x10^{15}$ ions/m^2s and a 250keV electron dose rate of $2.8x10^{22}$ e/m^2s for 9.2s and in (b) Ge irradiated with a 30keV Xe^+ ion dose rate of $5.0x10^{15}$ ions/m^2s and a 1MeV electron dose rate of $1.8x10^{23}$ e/m^2s for 4.5s. Each arrow in these micrographs indicates the diffraction vector of **g**=111.

Figure 4.2

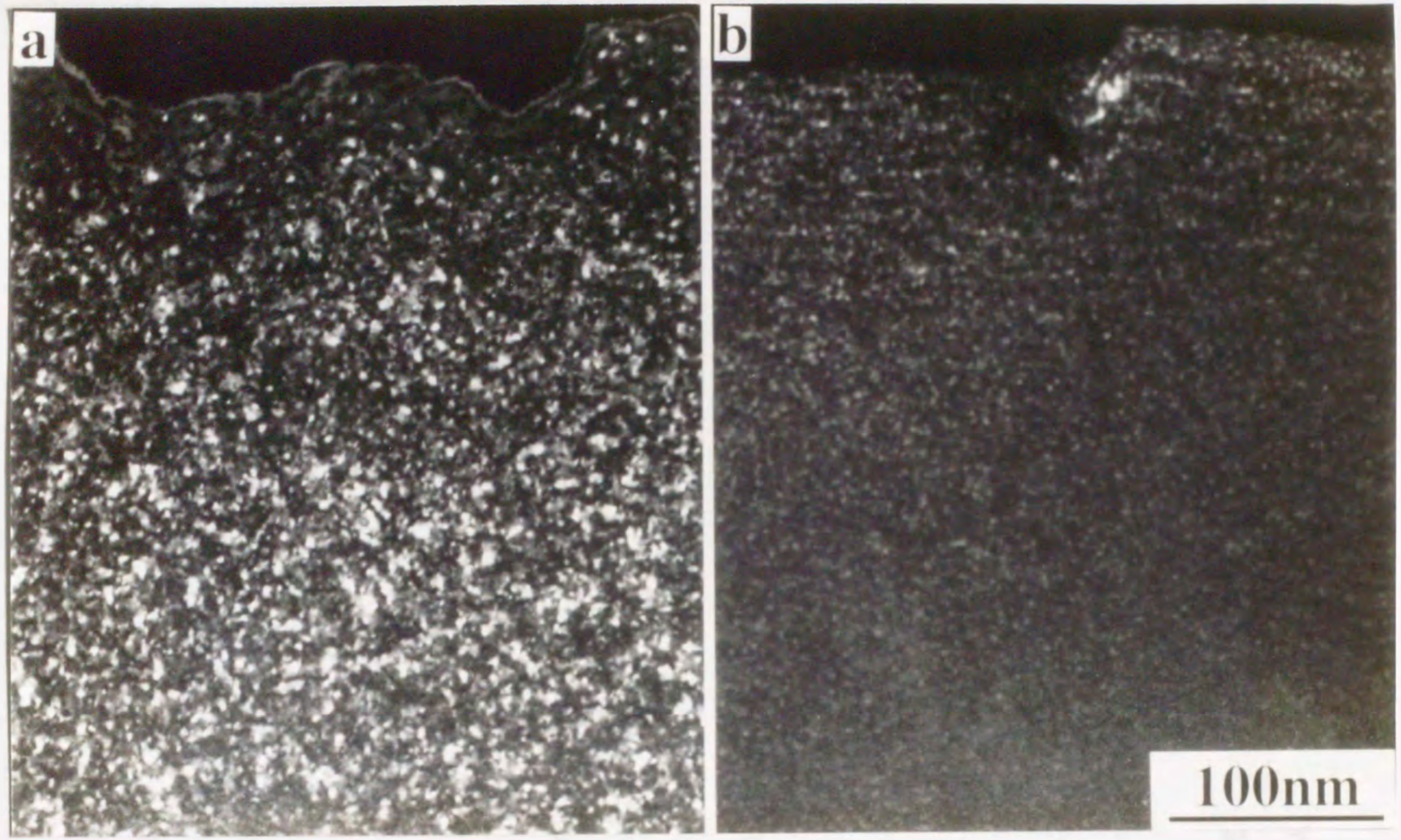

Figure 4.2 Weak-beam dark-field images showing I-loops observed in (a) MgO irradiated with a 30keV Xe^+ ion dose rate of $5.8x10^{15}$ ions/m^2s and a 1MeV electron dose rate of $2.9x10^{23}$ e/m^2s for 160s and in (b) $MgAl_2O_4$ irradiated with a 30keV Xe^+ ion dose rate of $9.4x10^{15}$ ions/m^2s and a 250keV electron dose rate of $2.9x10^{22}$ e/m^2s for 1940s.

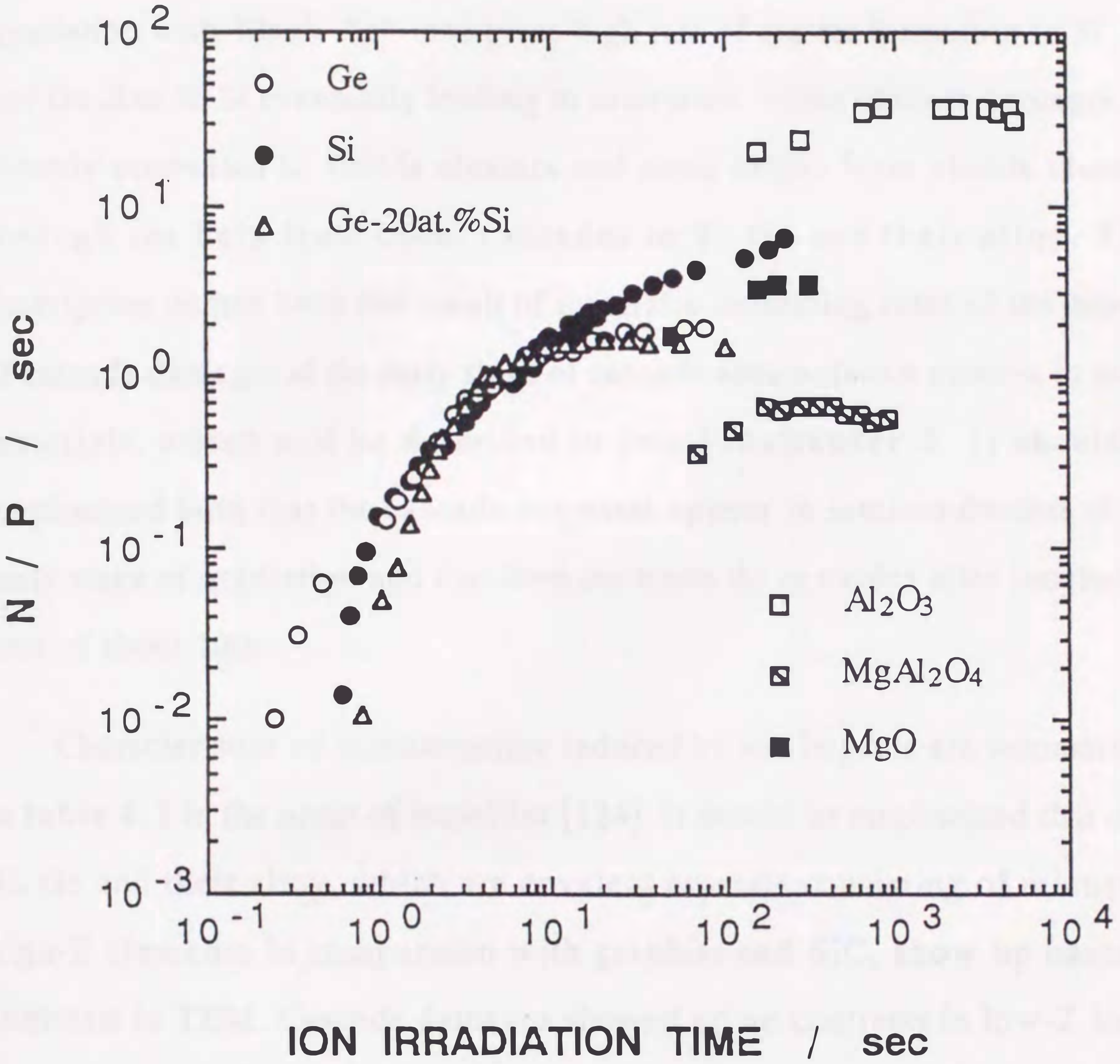

Figure 4.3 Variation of the area density of cascade contrasts, N, per ion dose rate, P, in Si, Ge and Ge-20at.% Si and that of I-loops, N, in α-Al_2O_3, MgO and $MgAl_2O_4$ per ion dose rate under irradiation with 30keV Xe^+ ions and 250keV or 1MeV electrons.

is adopted as the density, because the projected range [67] of 30keV Xe$^+$ ions is 20.3 nm in Si and 12.9 nm in Ge and is smaller than the specimen thickness. Irradiation with 30keV Xe$^+$ ions gives high rate of cluster formation in Si, Ge and Ge-20at.% Si eventually leading to saturation. Some cascade damages are directly converted to visible clusters and some others form visible clusters through the help from other cascades in Si, Ge and their alloy. This description comes from the result of quadratic increasing rates of the density of cascade damages at the early stage of cascade accumulation process in those materials, which will be described in detail in **chapter 5**. It should be emphasized both that the cascade contrasts appear in semiconductors at the early stage of irradiation and that loop contrasts do in oxides after incubation time of about 100s.

Characteristics of microstructure induced by ion impacts are summarized in **table 4.1** in the order of ionicities [124]. It should be emphasized that only Si, Ge and their alloy, which are covalent crystals consisting of relatively high-Z elements in comparison with graphite and SiC, show up cascade contrasts in TEM. Cascade damages showed up no contrasts in low-Z ionic crystals through TEM. A possible reason is described in the following way. In case of lower-Z crystals, the range of incident ions is long and it results in lower energy density within cascade regions, or in the lower concentration of point defects. Furthermore, the recombination of Frenkel pairs is predominant in ionic crystals because of the large spontaneous recombination volume, the high concentration of structural vacancies and so on. Namely, small number of point defects are rather homogeneously distributed in a cascade region in ionic crystals even when heavy-ions impact on crystals.

Table 4.1 Characteristics of microstrustural evolution in non-metallic inorganic crystals under dual-beam radiation of 30keV Xe^+ ions and 250 or 1000keV electrons. The results appeared in literatures are also shown with the references.

Specimen	Pauling's Ionicity	Microstructural Evolution	reference
Si	0	cascade	
Ge	0	cascade	
Ge-20at.% Si	0	cascade	
Ge-33at.% Si	0	cascade	
Graphite	0	amorphous	
GaAs	0.04	cascade	121,122
InP	0.04	cascade	123
SiC	0.12	amorphous	
WC	0.15	loop	
VC	0.18	loop	
TaC	0.22	loop	
TiC	0.22	loop	
HfC	0.30	loop	
α-Al_2O_3	0.59	loop	
ZrO_2	0.63	loop	
$MgAl_2O_4$	0.66	loop	
$SrTiO_3$	0.68	cascade	
MgO	0.73	loop	

Powder specimens of Si, Ge, Ge-20at.% Si and Ge-33at.% Si were irradiated with 40 and 60keV Nb^+ ions for getting more insights into the structure of cascade damages. **Figure 4.4** is typical examples of showing both structure factor and strain contrast in those crystals. Both kinds of white contrasts and black ones are seen in the same region of specimens, though they are not so-called black-and-white contrasts corresponding to dislocation loops. A possible reason is thought to be the following way: High energy ions produce point defects which distribute rather heterogeneously in a cascade damage depending on the combination of ion species and targets. **Figure 4.5** is an example of three-dimensional (3-D) profiles of point defects calculated from the TRIM-90 code [67], showing the distribution of point defects in Si irradiated with a 30keV Xe^+ ion. The cascade damages separate into small subcascade regions which are defined as localized regions of point defects. The average separation of subcascade region is about 1.6nm. The micrograph (**figure 4.4**(b)) was taken under the condition of g=111 and $s=0.4\ nm^{-1}$ which provided an effective extinction distance (ξ^{eff}=2.5 nm). Here, g and s are the diffraction vector and the deviation parameter, respectively. According to Edington [61], 0.25, 0.3, 0.7, 0.8 and $1.25\xi^{eff}$ in thickness give reverse of black-and-white contrasts of dislocation loops. In case of **figure 4.4** (b), those values correspond to 0.63, 0.75, 1.8, 2.0 and 3.1 nm in thickness which would cause reverse of contrasts. Some of defect clusters show black and white contrasts corresponding to loops in Ge-20at.% Si and Ge irradiated with 60keV Nb^+ ions. **Figure 4.6** shows the comparison of center dark field (CDF) images with deviation parameters (a) s=0 and (b) $s=0.4\ nm^{-1}$ in Ge irradiated with 60keV Nb^+ ions up to $5x10^{16}$ ions/m^2. Dot contrasts in (b) show structure factor contrasts which are attributable to amorphous, while

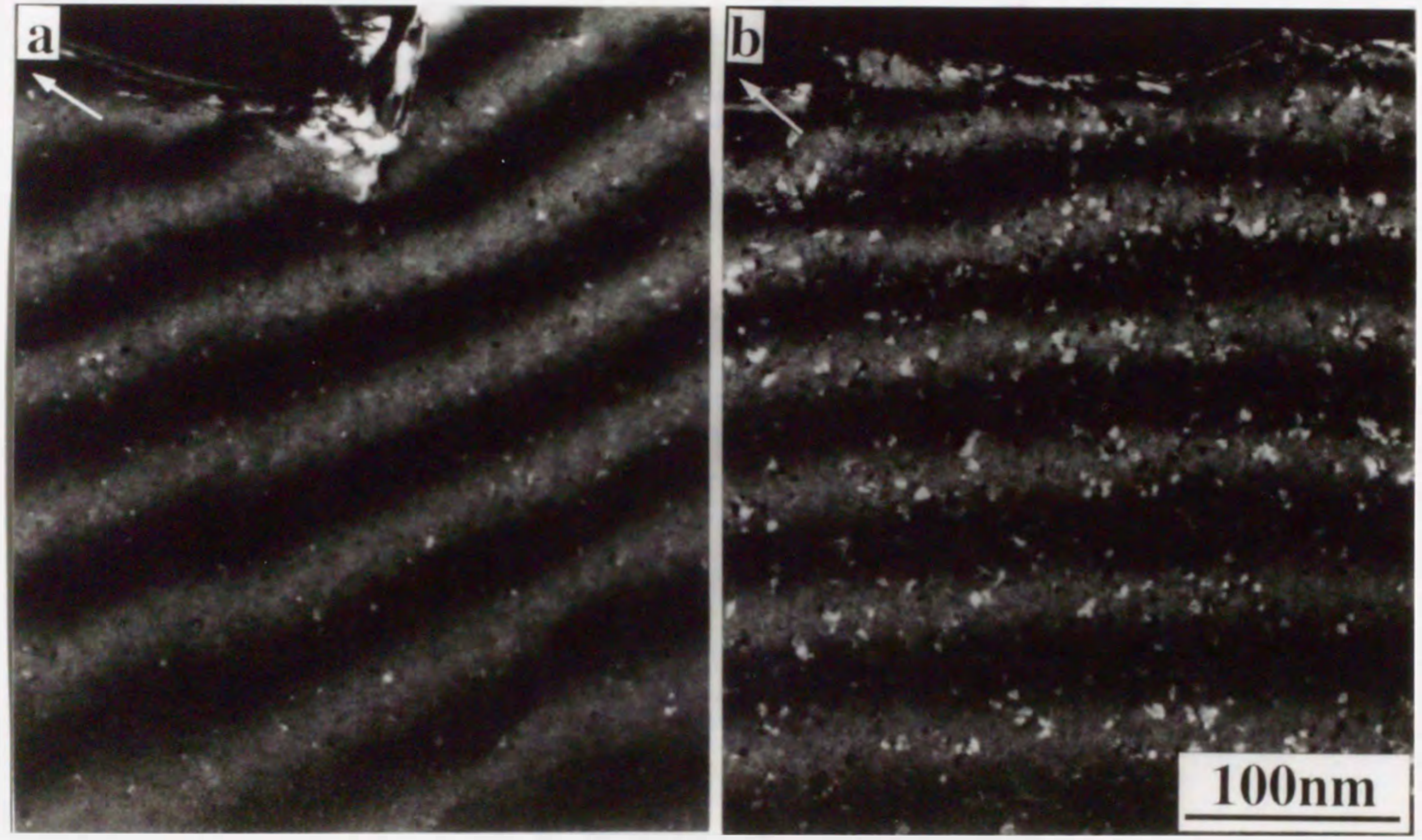

Figure 4.4 Weak-beam dark-field images showing cascade contrasts in (a) Si irradiated with a 60keV Nb^+ ion dose of 5.5×10^{16} ions/m^2 and in (b) Ge-20at.% Si irradiated with a 40keV Nb^+ ion dose of 4.9×10^{16} ions/m^2. Each arrow in these micrographs indicates the diffraction vector of **g**=111.

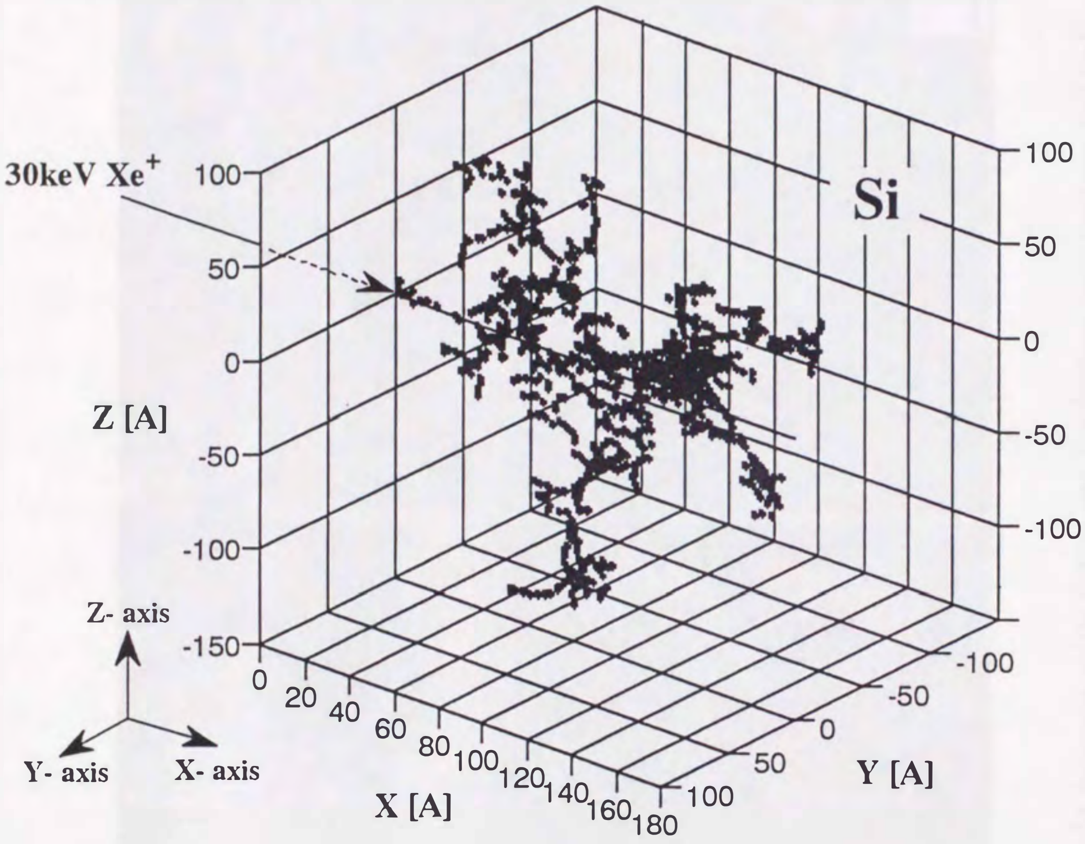

Figure 4.5 The three dimensional plot showing typical collisional trajectories for events with a 30keV Xe^+ ion in Si.

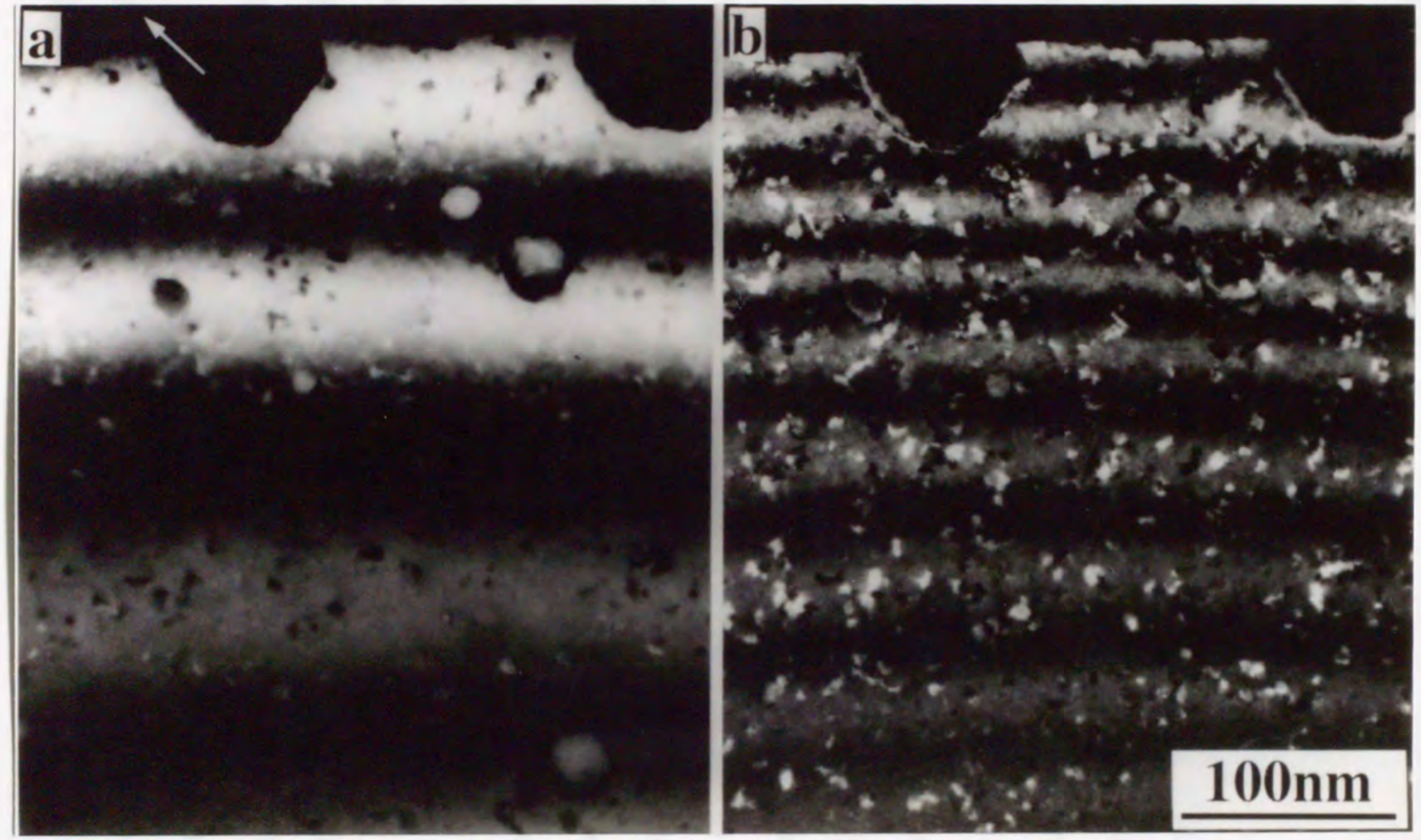

Figure 4.6 A comparison of dark-field images with different deviation parameters (a) $s=0$ and (b) $s=0.4\text{nm}^{-1}$ in Ge irradiated with a 60keV Nb^+ ion dose of $5.5\text{x}10^{16}$ ions/m^2. The arrow indicates the diffraction vector of $\mathbf{g}=111$.

those in (a) do structure factor and strain contrasts. Further careful investigation of these micrographs provides amorphous contrasts surrounded by strain contrasts as indicated with arrows in the micrographs.

Figure 4.7 compares the size distribution of those contrasts. As shown in the figure, one can see the diameter in WB image is larger than that of CDF or bright field (BF) image. These results let us conclude that cascade damages are essentially amorphous surrounded by strained region, or high concentration of point defects. A cascade produces a hot region in it where the average energy of each atom exceeds the melting points during thermal spike which is thought to be prolonged about 10^{-12}s in silicon. Interstitial atoms generated by collisional phase of cascades are distributed on the periphery of cascade damages where temperature is estimated to be about 500K in 5keV cascade in copper [72]. Hence, the thermal spike leaves an amorphous region surrounded by the strain region. The microstructure in Si irradiated to rather high dose (about 10^{17} ions/m^{2}s) indicates that cascade damages in Si are amorphous surrounded by disordered region [90,126,127]. Those disordered regions including amorphous phase anneal out at room temperature [128]. The annealing rate depends on ion species; 40% of cascades with low energy density, generated by light ions, anneal out after 15-30min, but non of cascades with high energy density disappears at room temperature. The annealing experiments in TEM [89,129], which will be shown later, also indicate the annealing resistance in case of heavy ion irradiation.

The structure of cascade damages depends strongly on the combination of ion species and target atoms. The diameter of cascade contrasts has been

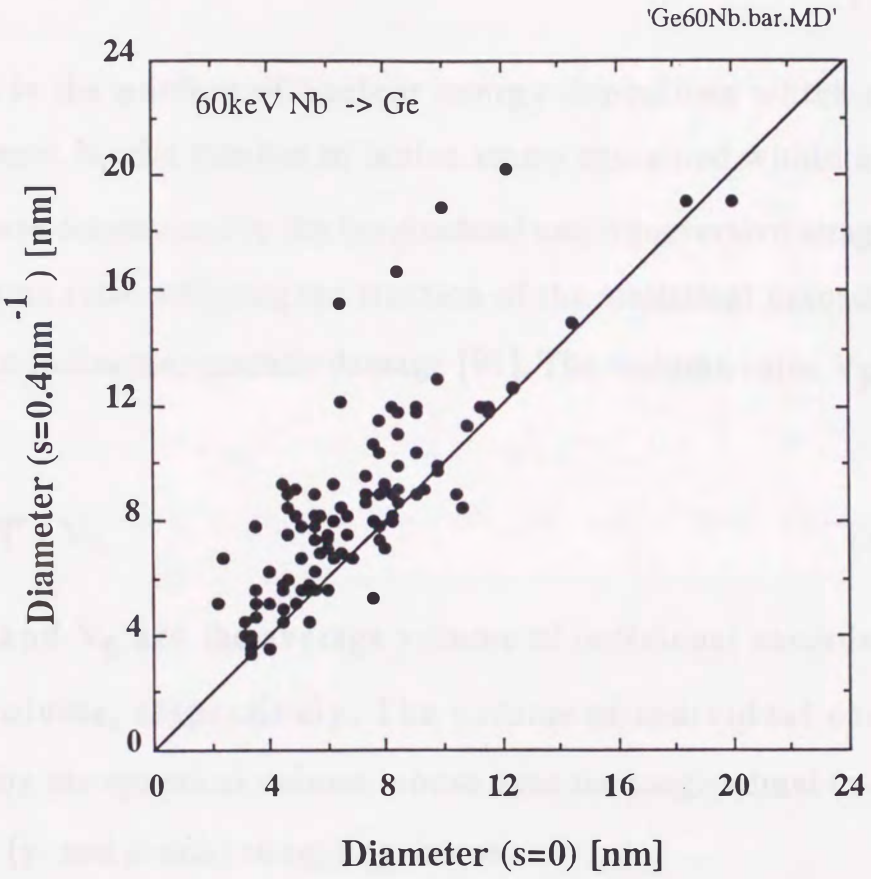

Figure 4.7 The relation between diameters of cascade contrasts in a dynamical DF (s=0) image and a weak-beam DF (s=0.4nm^{-1}) image. Cascade contrasts in the weak-beam DF image are larger than those in the dynamical one.

reported to depend on mass of projectiles [89,90,129]. The dependence was systematically examined in terms of the ratio of the average diameter of cascade contrasts to the transversive straggling of ions as a function of energy density. The energy density θ_v is described as

$$\theta_v = 0.2\,\nu(E) / N_v V_R, \qquad (4.1)$$

where $\nu(E)$ is the portion of nuclear energy deposition which results in collision events, N_v the number of lattice atoms contained within a spheroid whose axes are determined by the longitudinal and transversive straggling and V_R the volume ratio defining the fraction of the statistical cascade volume filled with an individual cascade damage [91]. The volume ratio V_R is given by

$$V_R = V_I^{av} / V_S, \qquad (4.2)$$

where V_I^{av} and V_S are the average volume of individual cascades and the transport volume, respectively. The volume of individual cascades is determined by the spherical volume whose axes are longitudinal (x-axis) and transversive (y- and z-axis) straggling, hence,

$$V_I = \frac{4\pi}{3}\left(\langle \Delta x^2\rangle_I \langle y^2\rangle_I \langle z^2\rangle_I\right)^{1/2}, \qquad (4.3)$$

where Δx is the straggling of x-axis and $<y^2>$ and $<z^2>$ are the y- and z-variances of the rest locations projected to the x-axis. The transport cascade volume, V_S, is described as a spheroid having longitudinal and transversive straggling, or

$$V_S = \frac{4\pi}{3}\langle \Delta x^2\rangle^{1/2}\langle y^2\rangle . \qquad (4.4)$$

Based on this treatment, the energy deposition density was calculated for the present experiments. The values of $\nu(E)$, V_I^{av}, N_v, θ_v and $2<y^2>^{1/2}$ are tabulated in **table 4.2**, together with the average diameter of cascade contrasts, $<D>$. The values of θ_v and $<D>/2<y^2>^{1/2}$ in **table 4.2** are plotted in **figure 4.8** (a) for Ge and in (b) for Si with the results appeared in literatures [89,90,129]. One can see the value of $<D>/2<y^2>^{1/2}$ increasing with the value of θ_v. The value of $<D>/2<y^2>^{1/2}$ becomes greater than unity at the higher energy density than about 1 and 3 eV/atom for Si and Ge, respectively. The results strongly suggest the importance of the parameter θ_v which is related with the structure and the stability of cascade damages. When $\theta_v>1$eV/atom, very large fractions of theoretical collision cascade (i.e., transport cascade) regions are rendered amorphous. In other words, thermal spikes in high energy density cascades extend amorphous regions over the transport cascade volume and even beyond it. In the case that $\theta_v<0.5$eV/atom, the formation of subcascades becomes significant. The subcascades are essentially amorphous surrounded by interstitial atoms, being invisible through bright field electron microscopy at the early stage of irradiation. Heavy ions, such as 30keV Xe^+ and 40keV Nb^+ ions, produce high energy density cascades (about 1 eV/atom). In this case, the mean free path of ions is small enough to produce an amorphous region over a cascade damage and a surrounded strain region. 30keV Ar^+ ions, on the other hand, produce relatively low energy density cascades (about 0.8 eV/atom) which produce rather large cascade damages and small amorphous regions surrounded by low strain regions.

Table 4.2 Values of the nuclear energy deposition, volume of individual cascades, the energy deposition density, diameter of the transport cascades and the average diameter of cascade contrasts in TEM. The calculated results are derived as the average value of 100 cascades with use of the TRIM-90 code.

Specimen	Ion	Energy [keV]	$\nu(E)$ [keV]	V_I^{av} [nm^3]	$\langle\theta_v\rangle$ [eV/atom]	$2\langle y^2\rangle^{1/2}$ [nm]	$\langle D\rangle$ [nm]
Si	Ar	60	41.3	113	0.15	17.4	4.2
Si	Nb	60	54.4	771	0.28	9.2	4.1
Si	Nb	40	36.6	260	0.56	7.1	4.0
Ge	Nb	60	55.6	375	0.67	9.8	6.7
Ge	Ar	30	21.7	118	0.71	10.8	4.6
Ge	Nb	40	37.3	186	0.90	7.2	4.9
Ge	Xe	30	26.6	112	1.07	4.2	6.3

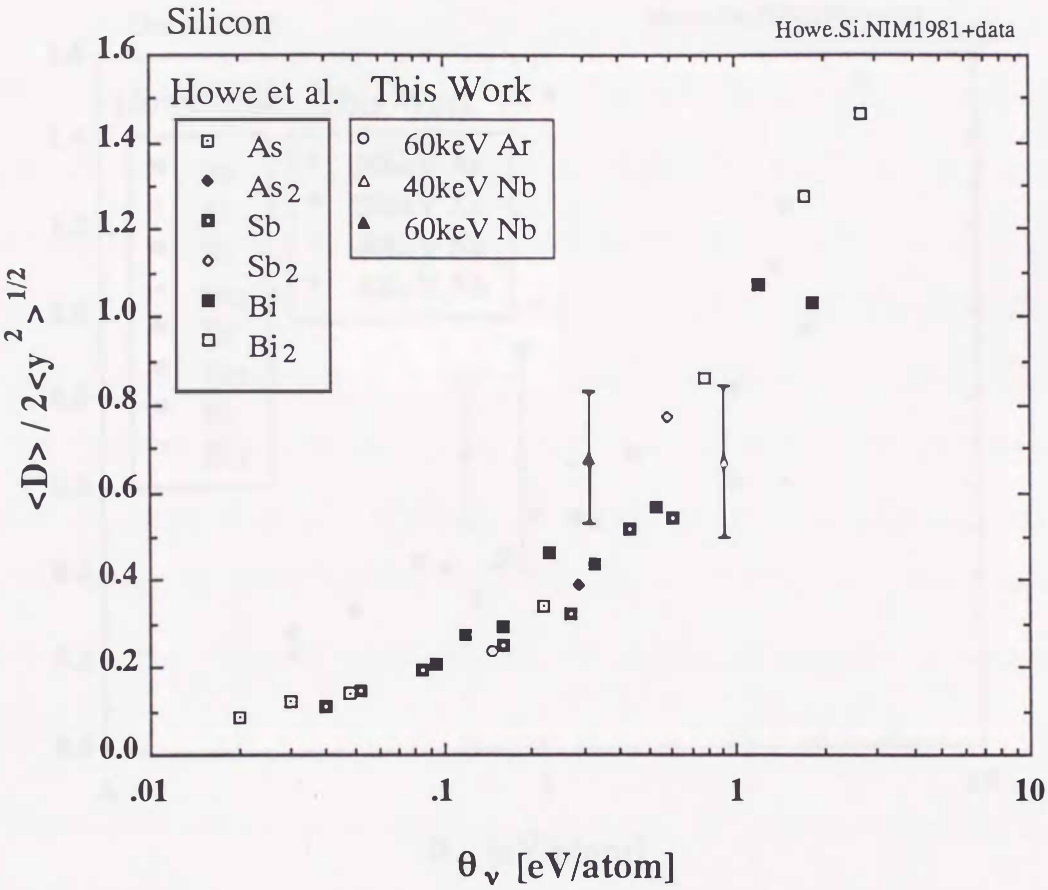

Figure 4.8 (a) The normalized diameter of cascade contrasts, $\langle D\rangle/2\langle y^2\rangle^{1/2}$, as a function of the deposition energy density, θ_v, for Si irradiated with As^+, Sb^+ and Bi^+ ions [90,91] and Ar^+, Nb^+ and Xe^+ ions.

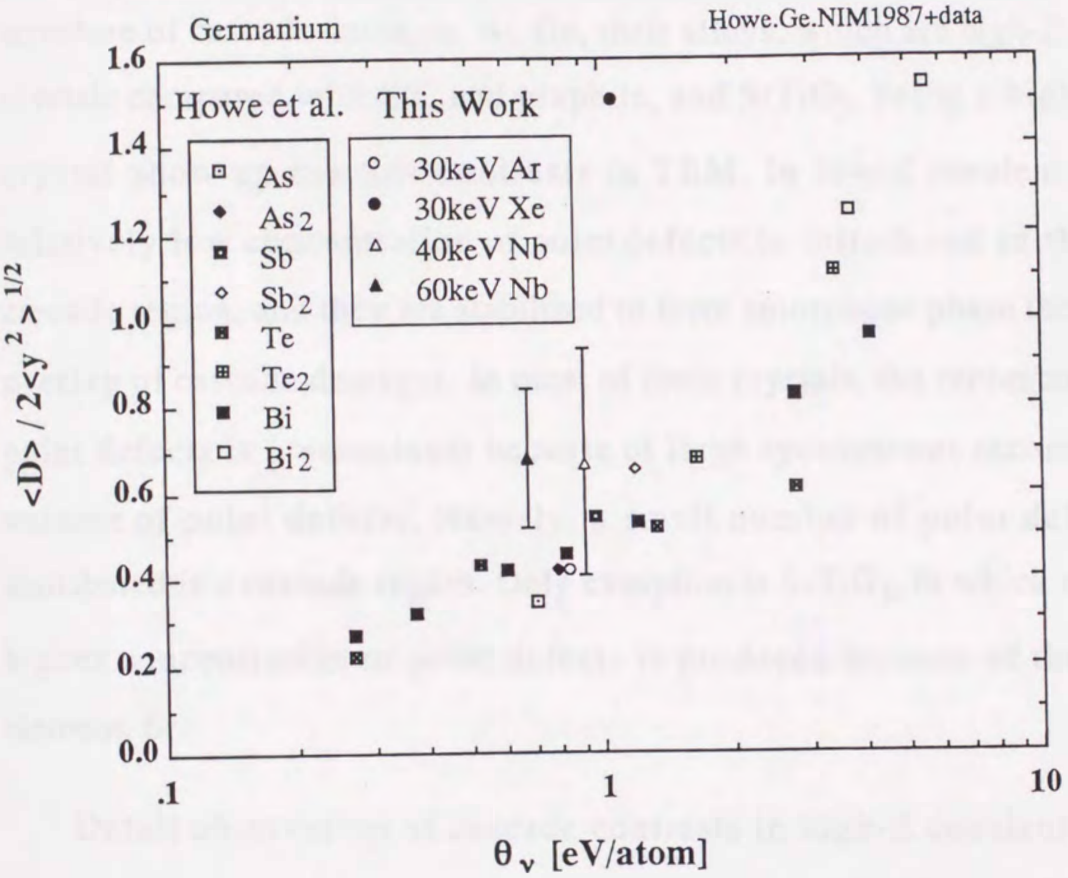

Figure 4.8 (b) Same as in (a), but for Ge irradiated with various kinds ions.

4.4 CONCLUSIONS

Irradiation with 30keV Xe^+ ions has been performed on non-metallic inorganic materials, such as ceramics and semiconductors to investigate the structure of cascade damages. Si, Ge, their alloys, which are high-Z covalent crystals compared with SiC and graphite, and $SrTiO_3$, being a high-Z ionic crystal show up cascade contrasts in TEM. In low-Z covalent crystals, relatively low concentration of point defects is introduced in the larger cascade region, and they are stabilized to form amorphous phase through the overlap of cascade damages. In most of ionic crystals, the recombination of point defects is predominant because of large spontaneous recombination volume of point defects. Namely, a small number of point defects are distributed in a cascade region. Only exception is $SrTiO_3$, in which relatively higher concentration of point defects is produced because of the high-Z element, Sr.

Detail observation of cascade contrasts in high-Z covalent crystals irradiated with 40 and 60keV Nb^+ ions has been further performed in kinematical ($\mathbf{s}\neq0$) and dynamical ($\mathbf{s}=0$) conditions. Cascade damages exhibit strong structure factor contrasts in the dynamical condition, which are consistent with amorphous regions. In the kinematical condition, on the other hand, cascade damages exhibit not only the structure factor contrasts but also the strain contrasts corresponding to regions having high concentration of interstitial atoms on the periphery of cascade damage. Furthermore, the diameters of cascade contrasts in the kinematical condition are larger than that in the dynamical one. The structure of cascade damages is, therefore, described as amorphous regions surrounded by strained regions. The ratio of the diameter of cascade contrasts in the kinematical condition to the diameter of transport cascades increases with increasing the energy density of cascade damages in Si and Ge. In addition, the value of <D> becomes far larger than that in the dynamical one as increasing the energy density of cascade damages in Ge.

CHAPTER 5

ACCUMULATION PROCESS OF CASCADE DAMAGES AND EFFECT OF CONCURRENT IRRADIATION WITH IONS AND ELECTRONS ON THE PROCESS IN SILICON AND GERMANIUM

5.1. INTRODUCTION

Neutron irradiation produces PKAs whose energy distributes widely from zero to the maximum; the maximum energy is estimated, for instance, as the order of MeV for 14MeV neutrons. The PKAs subsequently produce irradiation damages depending on their energy (T); those are cascade damages for T>keV and isolated point defects for $E_d<T<$keV. The PKAs also induce electronic excitation and athermal migration of point defects when $T<E_d$. Those irradiation induced processes simultaneously affect each other and cause synergistic effects in materials. Dual-beam irradiation with ions and electrons provides independent factors controlling irradiation damage processes. Thus, it gives important information on the concurrent or synergistic effect of point defects and cascade damages, and the structure and the stability of cascade damages in various irradiation environments. Heavy ions primarily generate cascade damages, and fast electrons induce isolated point defects, electronic excitation and athermal migration of point defects.

The objectives of this chapter are to clarify the accumulation process of cascade damages under concurrent irradiation with ions and electrons and to get insights into the concurrent effects of cascade damages and isolated point defects. The accumulation process of cascade damages is examined through in-situ observation under systematic dual-beam irradiation conditions. Kinetic equations which describe the accumulation of cascade damages under dual-beam irradiation are proposed. Through analyses of experimental results based on the kinetic equations, the accumulation of cascade damages and the concurrent effect are discussed. Further discussion is extended to the structure and the stability of cascade damages.

5.2. EXPERIMENTAL METHODS

The accumulation process of cascade damages in Ge and Si was examined under irradiation with 30keV Xe^+, 30keV Ar^+ or 60keV Ar^{2+} ions. Relatively low ion doses less than 10^{17}ions/m^2 were used with various ratios of the 1MeV electron dose rate (10^{22}~10^{23}e/m^{2}s) to the ion dose rate (~10^{15}ions/m^{2}s) at room temperature in the HVEM-ACC facility at KU.

As shown in chapter 3, the ions dose rate was measured with the Faraday cup which has an aperture with diameter of 200μm. The measured ion dose rates will be sometimes called 'nominal ion dose rate' hereafter. 'Actual ion dose rate' is defined as the net ion dose rate around areas observed. The actual ion dose rate cannot be measured experimentally but can be estimated theoretically. The words 'nominal' and 'actual' will be used in this chapter when the difference of them should be emphasized.

5.3. ACCUMULATION OF CASCADE DAMAGES IN SILICON AND GERMANIUM

Figure 5.1 shows sequential micrographs showing the accumulation process of cascade contrasts in Ge irradiated with 30keV Xe^+ ions and 1MeV electrons. Cascade damages show up their contrasts and increase in their number with irradiation time. The area density of cascade contrasts, N, in various specimens was examined during dual-beam irradiation with 30keV Xe^+ ions and 250keV or 1MeV electrons. A typical example of experimental results is shown in **figure 5.2**. The area density, which depends scarcely on the specimen thickness, is adopted as the density, because the projected range of 30keV Xe^+ ions is 20 nm in Si and 13 nm in Ge and it is smaller than the specimen thickness. Irradiation on Si, Ge and Ge-20at.% Si with 30keV Xe^+ ions gives high formation rates of cascade contrasts eventually leading to saturation. As shown in **figure 4.3**, one can see quadratic increasing rates of the density of cascade contrasts at the early stage of irradiation in those semiconductors. The initial slopes of the accumulation curves are determined to be about 1.3, 1.6 and 2.3 for Ge, Si and Ge-20at.% Si irradiated with 30keV Xe^+ ions, respectively. One can see relatively larger slope for Ge-20at.% Si. Solid solutions provide, in general, lower rate of electron and phonon transport and lower mobility of point defects in comparison with pure solids. These features may result in the different slopes of the accumulation process of cascade contrasts.

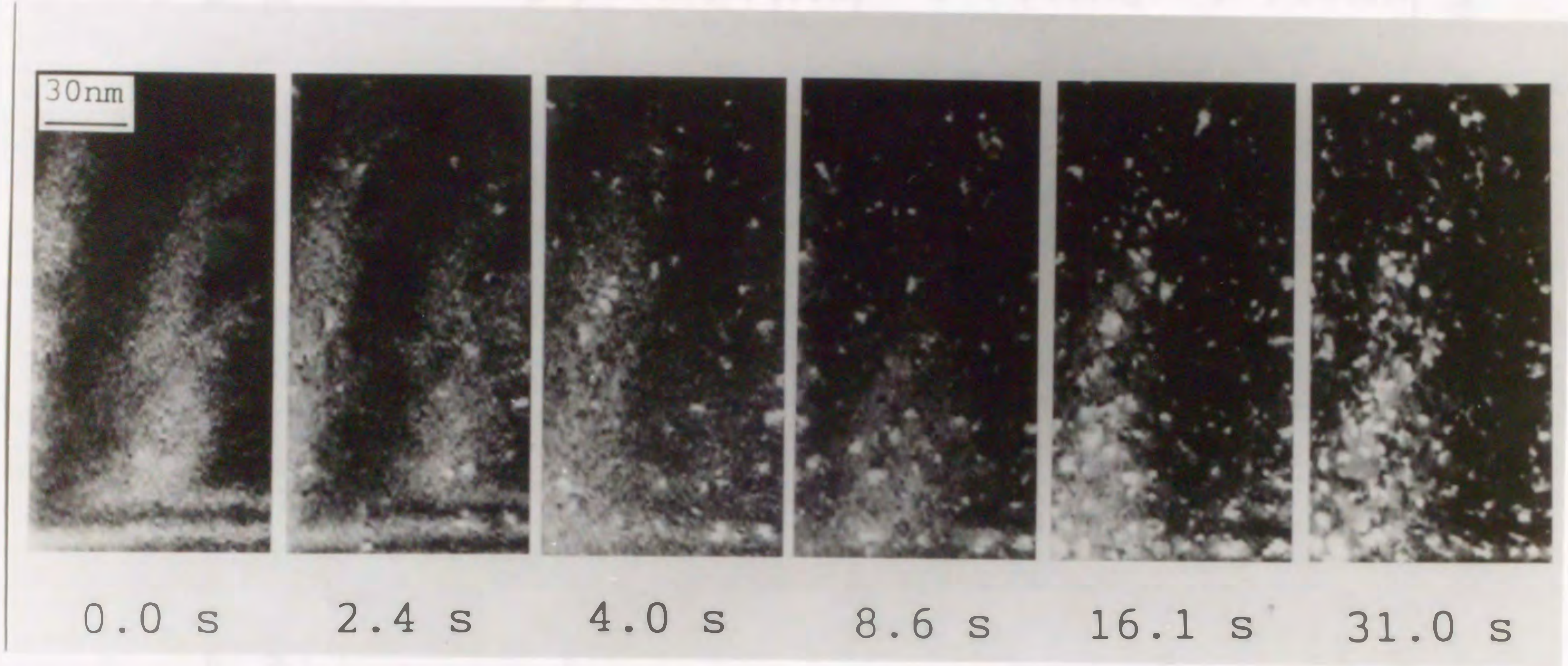

Figure 5.1 A sequence of weak-beam dark-field images on TV monitor through the imaging system, showing evolution of cascade contrasts in Ge irradiated with a 30keV Xe^+ ion dose rate of 5.0×10^{15} ions/m^2s and 1MeV electron dose rate of 1.8×10^{23} e/m^2s.

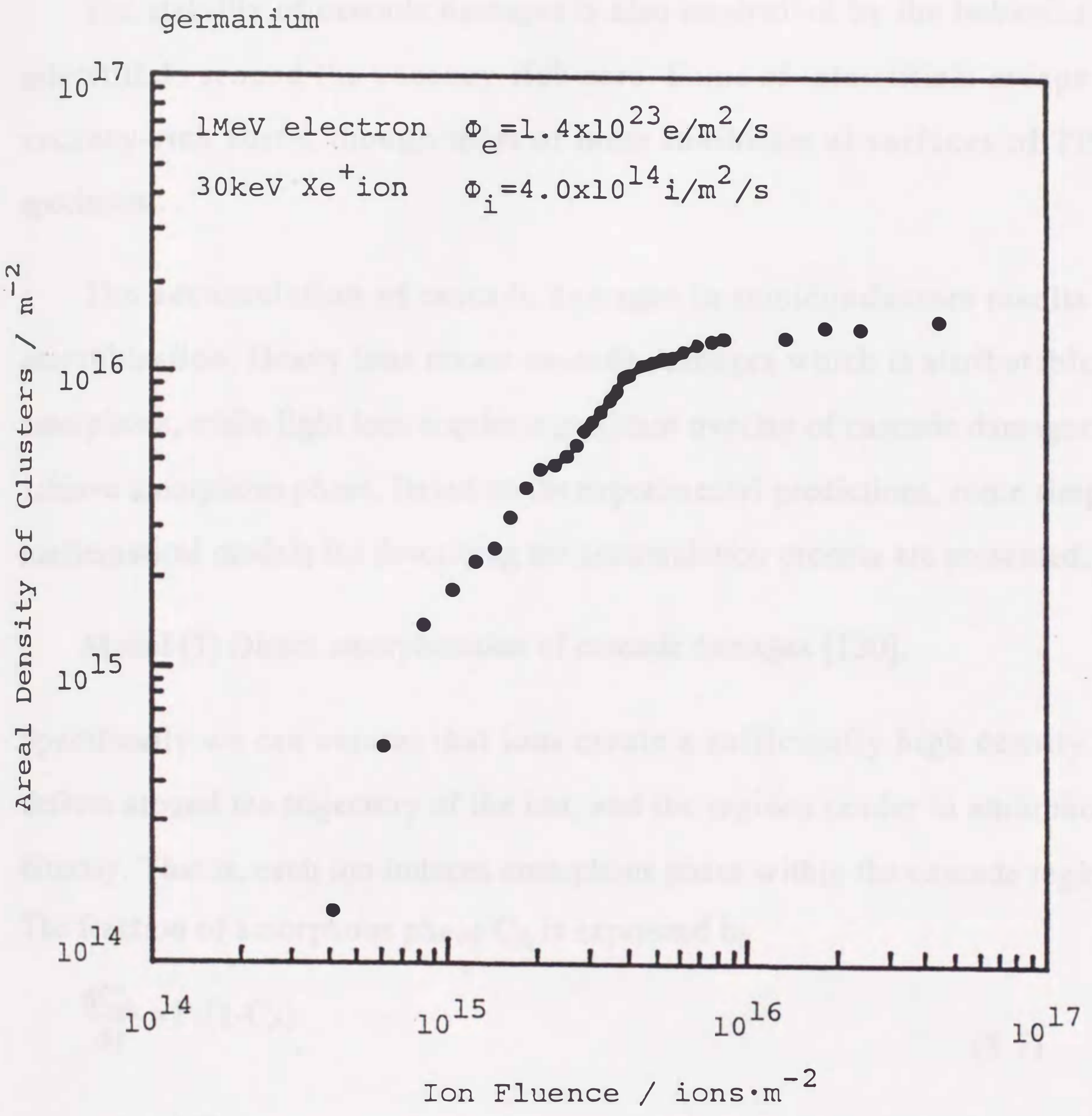

Figure 5.2 An example of accumulation of the area density of cascade contrasts in Ge under irradiation with a 30keV Xe^+ ion dose rate of $4.0x10^{14}$ ions/m^2s and a 1MeV electron dose rate of $1.4x10^{23}$ e/m^2s.

The stability of cascade damages is also controlled by the behavior of interstitials around the vacancy-rich core. Some of interstitials escape to vacancy-rich cores, though most of them annihilate at surfaces of TEM specimens.

The accumulation of cascade damages in semiconductors results in amorphization. Heavy ions create cascade damages which is attributable to amorphous, while light ions require significant overlap of cascade damages to achieve amorphous phase. Based on the experimental predictions, some simple mathematical models for describing the accumulation process are presented.

Model (1) Direct amorphization of cascade damages [130]:

Specifically we can assume that ions create a sufficiently high density of defects around the trajectory of the ion, and the regions render to amorphous directly. That is, each ion induces amorphous phase within the cascade region. The fraction of amorphous phase C_A is expressed by

$$\frac{dC_A}{dt} = P_i(1-C_A), \qquad (5.1)$$

where t and P_i are, respectively, irradiation time and the production rate of cascade damages. The solution of eq. (5.1) with the initial condition (C_A=0 at t=0) is

$$C_A = 1 - \exp(-P_i\, t). \qquad (5.2)$$

Figure 5.3 shows the values of C_A as a function of irradiation time, where eq. (5.2) is denoted as n=0. The meaning of n and c will be described later. It

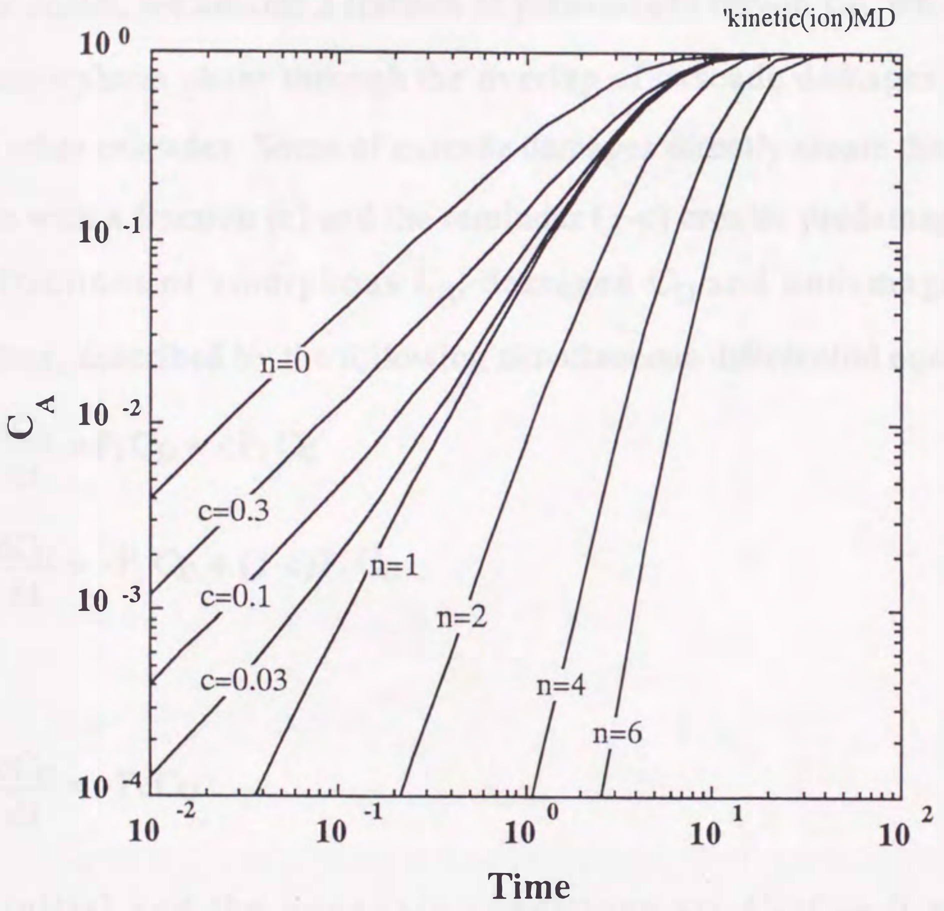

Figure 5.3 Fractional variation of fraction of amorphous phase, C_A, as a function of time for various combinations of c and n. The fraction of amorphous, C_A was calculated from eq.(5.2), (5.4) and (5.6).

shows that the fraction of amorphous region linearly increases as increasing ion dose eventually leading to saturation, i.e. completion of amorphization.

Model (2) Amorphization due to overlap of cascade damages:

In this model, we assume a fraction of predamaged region C_D, which becomes into amorphous phase through the overlap of cascade damages or the help from other cascades. Some of cascade damages directly create the amorphous region with a fraction (c) and the reminder (1-c) creates predamaged regions. The fractions of amorphous C_A, damaged C_D and undamaged C_U are, therefore, described by the following simultaneous differential equations,

$$\frac{dC_A}{dt} = P_i C_D + cP_i C_U , \tag{5.3a}$$

$$\frac{dC_D}{dt} = -P_i C_D + (1-c)P_i C_U \tag{5.3b}$$

and

$$\frac{dC_U}{dt} = -P_i C_U . \tag{5.3c}$$

The initial and the boundary conditions are $C_A=C_D=0$ at $t=0$ and $C_A+C_D+C_U=1$. Eq.(5.1) corresponds to eq.(5.3) with c=1. The solution of the simultaneous differential equations for C_A is

$$C_A = 1 - \left(1 + (1-c) P_i t\right) \exp\left(-P_i t\right). \tag{5.4}$$

Model (3) Amorphization due to n-tuple overlaps of cascade damages:

A straightforward extension of eq.(5.3) can be developed to cases where n-tuple overlaps of cascade damages are required for inducing amorphous phase.

The fractional damaged region generated by m-tuple cascade damage overlaps is C_m, is expressed by the simultaneous differential equations,

$$\frac{dC_A}{dt} = P_i\, C_{n-1}\ ,$$
$$\frac{dC_{n-1}}{dt} = -\, P_i\, C_{n-1} + P_i\, C_{n-2},$$
$$\frac{dC_{n-2}}{dt} = -\, P_i\, C_{n-2} + P_i\, C_{n-3},$$
$$\cdots\cdots\cdots$$
$$\cdots\cdots\cdots$$
$$\frac{dC_2}{dt} = -\, P_i\, C_2 + P_i\, C_1,$$
$$\frac{dC_1}{dt} = -\, P_i\, C_1 + P_i\, C_U$$

and

$$\frac{dC_U}{dt} = -P_i\, C_U \quad . \tag{5.5}$$

The solution of C_A of eq.(5.5) is derived as

$$C_A = 1 - \sum_{k=0}^{n} \frac{(P_i t)^k}{k!} \exp(-P_i t) \quad . \tag{5.6}$$

The values of C_A are calculated from eqs.(5.2), (5.4) and (5.6) with various combinations of n and c, and are shown in **figure 5.3**. At the initial stage of irradiation, the variation of C_A can be approximately expressed by $(P_i t)^x$. As the fraction of direct amorphous formation (c) becomes higher, the value of the power (x) becomes smaller. The values of c and n are strongly related to the power x, and phenomenologically related to the structure of cascade damages. That is, the higher energy density cascades leave the more stable and the larger amorphous region, and they develop into amorphous with the less number of overlaps. On the contrary, the structure of the lower energy density cascades is described as rather homogeneously distributed point defects within cascade regions, which develop into amorphous through the more number of overlaps of cascade damages. In order to describe the accumulation process of amorphous phase under dual-beam irradiation, the model (2) and the model (3) will be extended to the kinetic equations under dual-beam irradiation in the following section.